remote sensing

MDPI

Article

Time-Series InSAR-Constrained Spatiotemporal Evolution and Driving Factors of a Loess Landslide: A Case Study of the Li-Kan Highway Landslide on the Loess Plateau

Yue Wang [1], Yuxin Zhou [2], Zhaojun Pang [2,*], Haoran Gao [2], Xiaoyu Liu [2] and Wu Zhu [2]

[1] School of Highway, Chang'an University, Xi'an 710054, China; ywang@chd.edu.cn
[2] School of Geological Engineering and Geomatics, Chang'an University, Xi'an 710054, China; 2022226027@chd.edu.cn (Y.Z.); 2025226053@chd.edu.cn (H.G.); 2022026024@chd.edu.cn (X.L.); zhuwu@chd.edu.cn (W.Z.)
* Correspondence: pzjun@chd.edu.cn

Highlights

What are the main findings?

- Ascending- and descending-track time-series InSAR combined with APF reconstruction reveals pronounced three-dimensional kinematic heterogeneity of the Li-Kan Highway landslide, with predominantly northeastward motion and asynchronous deformation activity among different slope sectors.
- Rainfall–deformation associations show spatially variable lags of approximately 12–108 days, while a Massflow frontal-failure scenario yields a maximum simulated velocity of about 22.6 m/s and potential runout toward the slope toe and reservoir shoreline.

What are the implications of the main findings?

- The results demonstrate that the Li-Kan Highway landslide should be interpreted as a system of spatially differentiated and temporally asynchronous kinematic units rather than as a single block undergoing uniform deformation-stage transitions.
- The integrated framework linking three-dimensional InSAR deformation, CSDI-based activity identification, rainfall-response analysis, and dynamic runout simulation provides a practical approach for identifying active sectors and assessing the potential hazards of large loess landslides.

Abstract

Loess landslides exhibit strong spatial heterogeneity and complex rainfall responses, making their evolution difficult to characterize from one-dimensional deformation observations alone. This study investigates the Li-Kan Highway landslide on the right bank of the Lijiaxia Reservoir, China, by integrating ascending- and descending-track time-series InSAR, aspect-parallel flow (APF) constrained three-dimensional deformation reconstruction, the Comprehensive Standardized Deformation Index (CSDI), wavelet-based rainfall-response analysis, and Massflow numerical simulation. The reconstructed deformation field shows that the landslide is dominated by northeastward horizontal motion, while local sectors exhibit distinct movement directions and deformation components, indicating multiple kinematic units. Along the approximately 2 km P–P′ profile, the north–south, east–west, and vertical deformation–velocity components exhibit spatially variable patterns, consistent with heterogeneous slope kinematics. Principal component analysis shows that the first two components explain 85.6% of the total variance, summarizing the spatial variability. CSDI analysis of representative points P1–P3 reveals asynchronous deformation activity: P1 is mainly active in autumn 2018, P2 shows enhanced activity in 2019 and spring–summer 2020,

Check for updates

Academic Editor: Cristiano Tolomei

Received: 3 September 2026
Revised: 15 November 2026
Accepted: 17 November 2026
Published: 20 November 2026

Copyright: © 2026 by the authors. Licensee MDPI, Basel, Switzerland. This article is an open access article distributed under the terms and conditions of the Creative Commons Attribution (CC BY) license.

and P3 exhibits a weaker local increase around mid-2021. In particular, the 2020 response at P2 is interpreted as a local kinematic adjustment rather than synchronous acceleration of the entire slope. Because no overall failure occurred during the observation period, CSDI-defined Stage III is treated as enhanced deformation activity rather than a direct failure criterion. Continuous wavelet transform and time-lag cross-correlation indicate significant rainfall-related temporal responses, with deformation lagging rainfall by approximately 12, 108, and 36 days at P1, P2, and P3, respectively. Massflow simulation of a potential frontal failure scenario shows a rapid transition from source-area release to channelized high-speed runout and frontal deposition. The maximum simulated velocity reaches approximately 22.6 m/s in the main transport channel, while the frontal deposit exceeds 16 m in thickness and remains about 13.6 m at 200 s. The total simulated mass decreases by only about 0.38%, indicating good numerical mass conservation. These results demonstrate that the Li-Kan Highway landslide evolves through spatially heterogeneous and temporally asynchronous deformation, with rainfall responses varying among slope sectors. The integrated framework links long-term deformation monitoring, stage identification, rainfall-response analysis, and potential failure simulation, providing a practical basis for interpreting the evolution and hazard potential of large loess landslides.

Keywords: loess landslide; time-series InSAR; three-dimensional deformation; CSDI; rainfall response; Massflow; failure simulation

1. Introduction

Loess is characterized by a loose and porous structure, well-developed vertical joints, and water-induced collapsibility. Disturbances such as rainfall infiltration, reservoir-level fluctuations, earthquakes, and engineering excavation can therefore trigger progressive failure or even rapid long-runout sliding [1–3]. The Loess Plateau and its adjacent transition zones contain dense settlements, transport corridors, and hydraulic engineering infrastructure. Landslides can directly disrupt roads, damage buildings, and cause casualties, and may also block rivers, form landslide dams, and initiate cascading hazards. As extreme rainfall events become more frequent and major engineering construction continues, detecting concealed deformation and clarifying the spatiotemporal evolution and driving mechanisms of loess landslides are essential for improving early warning, optimizing engineering mitigation, and enhancing regional resilience.

Conventional remote-sensing investigations of landslides mainly rely on aerial photographs and multi-temporal optical satellite imagery. Manual interpretation or change detection based on tone, texture, morphology, and land-cover changes can rapidly establish landslide inventories and delineate landslide boundaries, cracks, and deposits [4,5]. However, optical observations are constrained by clouds, fog, shadows, snow, vegetation, and illumination conditions. They are less effective for detecting slowly moving landslides with weak surface signatures and usually record geomorphic responses after failure rather than continuously quantifying millimeter- to centimeter-scale pre-failure displacement. Interferometric Synthetic Aperture Radar (InSAR) retrieves surface deformation from phase differences between SAR acquisitions. Time-series approaches, including persistent scatterer and small-baseline subset methods, further reduce temporal and spatial decorrelation and atmospheric delays, enabling all-weather, day-and-night, wide-area monitoring with millimeter-level precision [6–9]. Consequently, InSAR has expanded from landslide detection to slow-deformation monitoring and reconstruction of historical deformation processes [10,11]. Recent regional applications further show that ascending- and descending-track time-series InSAR can support semi-automated landslide detection along

transportation corridors, while the joint use of single- and multi-look phases improves measurement-point coverage for deformation characterization in complex mountainous terrain [12,13]. In our previous study, we established an active-landslide inventory for the Longyangxia–Liujiaxia reach of the upper Yellow River by integrating ascending- and descending-track SBAS-InSAR observations with deep-learning-assisted landslide identification [14]. The integration of multi-track and multi-band SAR observations can further recover three-dimensional deformation fields and displacement records spanning more than a decade, supporting the identification of spatially differentiated motion and long-term creep [15]. Nevertheless, conventional InSAR products mainly measure one-dimensional displacement along the satellite line of sight (LOS) and remain affected by geometric sensitivity, phase-unwrapping errors, and low coherence.

Although time-series InSAR has substantially improved landslide deformation monitoring, most studies focus on annual deformation rates, point-based displacement curves, or local kinematic features. Spatial zoning, three-dimensional motion, and deformation stages are often analyzed separately, making it difficult to reveal the migration of deformation stages among slope sectors and their coordinated evolution [10,11,16]. Saito established the classical theoretical basis for forecasting landslide failure time from creep behavior [17]. Subsequent approaches include stage analysis based on spatiotemporal evolution [18], the improved tangent angle [19], association rules [20], optimal partitioning of ordered samples [21], inverse logistic functions [22], curve feature points [23], and spatial evaluation using displacement–rate ratios [24]; however, these methods can remain sensitive to sampling intervals, short-term fluctuations, and empirical thresholds. More recently, Zhang et al. [25] proposed the Comprehensive Standardized Deformation Index (CSDI), which fits a skewed probability distribution to InSAR deformation velocities and applies an equal-cumulative-probability transformation to map velocity into a dimensionless standard-normal metric. For the nearly 30-year Xinpu landslide record, this approach reduced overestimation of the acceleration stage compared with tangent-angle and velocity-ratio methods [26]. Joint analyses of multi-source monitoring data and slope stability have shown that external triggers can produce spatially differentiated deformation and stability evolution [27]. InSAR combined with wavelet analysis has also been used to identify landslide responses to seasonal rainfall [28], while coupling hydrological triggers with multi-temporal InSAR can extract transient slope-instability characteristics [29]. Time-series InSAR analysis of the Dandu ancient landslide further revealed seasonal rainfall-driven acceleration with a response lag of several weeks, highlighting the delayed hydrological control on slope deformation [30]. However, CSDI validation has mainly focused on representative points of reservoir landslides; whole-slope stage mapping and spatial migration analysis for loess landslides remain insufficiently explored.

Remote-sensing observations can characterize surface motion before failure but cannot directly reconstruct the dynamic process from initiation and acceleration to runout and deposition. Limit-equilibrium, finite-element, discrete-element, and depth-averaged continuum models are therefore widely used to investigate failure mechanisms, runout paths, and impact areas. Starting from the Savage–Hutter single-phase shallow granular-flow model [31], Hungr's equivalent-fluid runout model [32], and Iverson's physical framework for debris flows [33], subsequent work extended to coupled solid–fluid motion over three-dimensional terrain [34], generalized two-phase flow models [35], and open-source propagation platforms such as r.avaflow [36]. In engineering applications, depth-averaged models such as DAN3D simulate rapid landslide motion over complex three-dimensional terrain under different rheological laws [37,38]. Ouyang et al. [39] developed Massflow-2D using depth-integrated mass and momentum conservation equations and a MacCormack–TVD finite-difference scheme, and validated the model using cases including a Hong Kong

landslide and the Nora debris flow. The model was later extended to incorporate erodible beds and different rheological relationships and applied to dynamic back-analysis of debris flows in the Wenchuan earthquake area and the 2015 Shenzhen landfill landslide [40,41]. Multi-orbit InSAR observations have also been used to constrain active landslide thickness and simulate failure motion [42], demonstrating the potential of coupling remote sensing with dynamic models. An integrated study combining time-series InSAR, topographic change detection, rainfall analysis, and numerical simulation also demonstrated the value of linking pre-failure deformation with post-failure movement reconstruction for rotational landslides [43]. Existing Massflow studies can output flow depth, velocity, impact intensity, and deposition extent, but the results are sensitive to the initial landslide geometry and rheological parameters. InSAR-constrained failure simulation of loess landslides therefore remains limited.

The Li-Kan Highway landslide is located on the right bank of the Lijiaxia Reservoir in the upper Yellow River and is a typical large engineering-disturbed loess–mudstone interface landslide. Highway excavation altered the original slope geometry and stress state. The overlying loess is highly fractured and permeable, whereas the underlying mudstone is relatively impermeable; infiltrating water can therefore accumulate near the loess–mudstone interface and weaken the potential shear zone. Previous studies show that the landslide has undergone persistent long-term creep, with pronounced differences in movement direction and rate among slope sectors, and contains secondary sliding masses and local locked zones, indicating strong spatial heterogeneity [44]. The coexistence of long-term creep and local acceleration makes this landslide a representative case for investigating stage transitions and potential rapid failure of loess slopes.

Accordingly, this study investigates the Li-Kan Highway landslide by sequentially analyzing three-dimensional motion, deformation-stage evolution, rainfall response, and potential failure dynamics. First, ascending- and descending-track time-series InSAR observations are integrated with aspect constraints to reconstruct the three-dimensional deformation field and reveal spatial differences in movement direction among slope sectors. Second, CSDI is used to identify deformation stages for different spatial units, construct multi-temporal stage maps, and track the formation and migration of accelerated-deformation zones. Continuous wavelet analysis is then combined with time-lag cross-correlation to examine multi-scale deformation–rainfall relationships and compare rainfall responses among kinematic zones and deformation stages. Finally, high-activity areas identified from the three-dimensional deformation field and CSDI are used to define potential failure scenarios, and Massflow is applied to simulate post-failure velocity, runout paths, and deposition extent. This workflow links long-term deformation detection, stage-transition identification, external driving-factor analysis, and potential failure assessment to improve understanding of the evolutionary mechanism and support risk mitigation for the Li-Kan Highway landslide.

2. Study Area and Data

2.1. Study Area

The regional InSAR survey covers the upper Yellow River corridor from Longyangxia to Liujiaxia, extending across eastern Qinghai Province and western Gansu Province at the transition between the Tibetan Plateau and the Loess Plateau (approximately 35.2–36.3°N, 100.1–104.0°E). Elevations generally range from about 1600 to 4800 m. The terrain is characterized by alternating gorges and basins: major gorges include Longyangxia, Lijiaxia, and Liujiaxia, whereas the Guide and Xunhua basins contain well-developed multilevel fluvial terraces. The surrounding relief is controlled mainly by the Ela, Riyue, and Laji mountain ranges. Ascending- and descending-track Sentinel-1A data have been processed

for this regional domain to derive wide-area InSAR deformation products. Within this regional framework, the Li-Kan Highway landslide is selected as a representative case study for detailed three-dimensional deformation, temporal-evolution, rainfall-response, and potential-failure analyses.

The Li-Kan Highway landslide is located in Jianzha County, Huangnan Tibetan Autonomous Prefecture, Qinghai Province, China, on the right bank of the Lijiaxia Reservoir. The Lijiaxia–Kanbula tourist highway connects the reservoir area with Kanbula National Forest Park [45]. Highway excavation at the slope toe in 2002 disturbed slope stability; slide-resistant piles and structural beams were subsequently installed to restrain movement. Fissures and localized collapses have been reported since 2014, together with damage to retaining walls, drainage facilities and other stabilization structures [16,46]. The highway centerline, reservoir shoreline, mapped landslide boundary, representative cracks, rear scarp and approximate mitigation zones are shown in Figure 1b. The Lijiaxia Reservoir has a normal water level of 2180 m a.s.l. and operates under daily regulation [47]. The reference reservoir water surface is shown in Figure 1c to place the lower slope and slope toe in their topographic context.

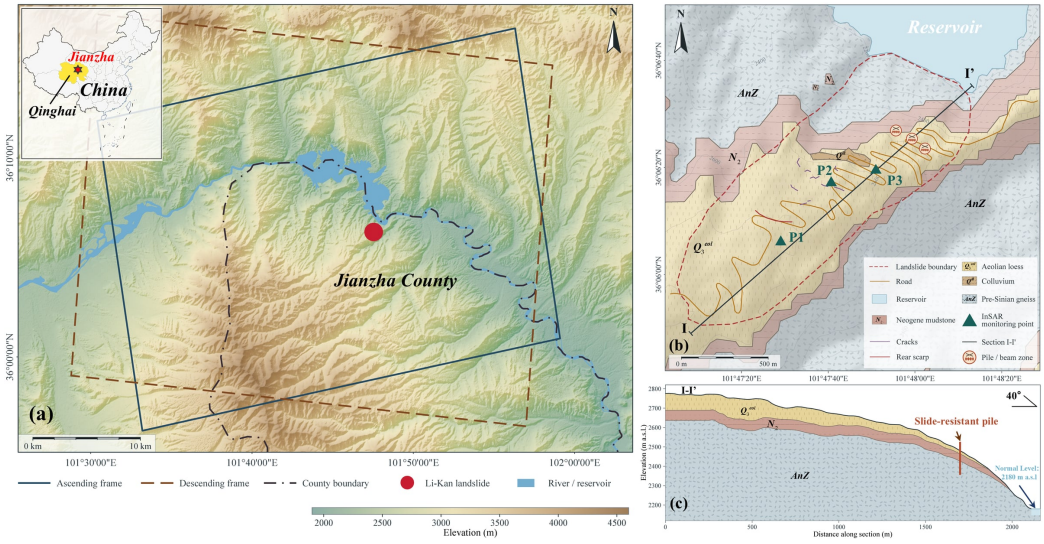


Figure 1. Location and engineering-geological setting of the Li-Kan Highway landslide. (**a**) Regional shaded-relief map with Sentinel-1 coverage, the county outline, river/reservoir and a national-location inset. (**b**) Interpretive engineering-geological map showing the landslide boundary, highway, reservoir shoreline, representative cracks and rear scarp, approximate mitigation zones, section I–I′ and InSAR monitoring points P1–P3. (**c**) Simplified overview section I–I′, with the ground profile and the 2180 m reference reservoir water surface. Geological contacts and pile geometry are schematic, based on the published stratigraphic and engineering setting [16,46]; pile length is not to scale.

The northeast-facing slope is developed in a layered rock–soil setting. The reported stratigraphic sequence comprises Upper Pleistocene aeolian loess, Neogene mudstone and older gneiss, with local colluvial deposits [16,46]. The loess–mudstone contact has been identified in previous site investigations as a potential preferential sliding interface [46]. Figure 1b,c provide an interpretive engineering-geological map and a simplified overview section I–I′. The section provides topographic context, whereas geological contacts and pile geometry are schematic representations of the published geological and engineering setting, rather than new measured geological boundaries or pile dimensions.

A separate experimental profile, P–P′, was defined for subsequent deformation analysis. The separate geological section I–I′ in Figure 1c was drawn using the geological information reported by Du et al. [16]. The full DEM-sampled P–P′ transect extends approximately 2 km,

with elevations of approximately 2224–2822 m. These profile elevations do not represent independently verified minimum and maximum elevations of the landslide body.

P1, P2 and P3 in Figure 1b identify the InSAR monitoring locations used for the displacement, deformation-stage and rainfall-response analyses. These locations lie within the mapped landslide boundary and outside the mapped reservoir water body. They are distinct from the numerical-simulation sampling locations, which are designated M1, M2 and M3 in Section 5.3 and represent the source area, main transport channel and frontal deposition zone, respectively. The P labels are reserved for InSAR monitoring and the M labels for simulation sampling.

Based on the active-landslide inventory that we previously established for the Longyangxia–Liujiaxia reach of the upper Yellow River [14], this section presents the regional spatial context of the Li-Kan Highway landslide. The previously published inventory comprises 963 mapped active landslides. Figure 2 depicts this established regional distribution, with active landslides concentrated along both banks of the Yellow River and exhibiting pronounced river-corridor clustering. Within this regional pattern, the Li-Kan Highway landslide was selected as a representative case for subsequent analyses of three-dimensional deformation, deformation-stage evolution, rainfall response, and potential failure.

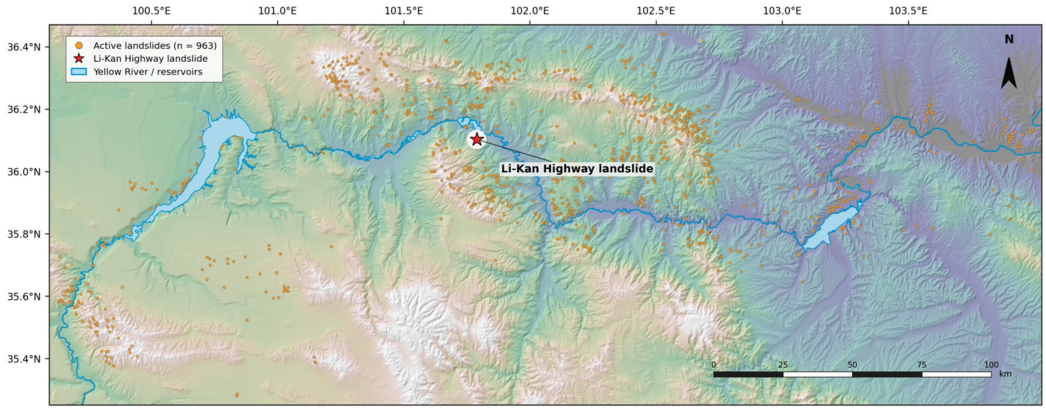


Figure 2. Regional distribution of 963 active landslides previously identified along the upper Yellow River from Longyangxia to Liujiaxia and the location of the Li-Kan Highway landslide.

2.2. Data

Sentinel-1A Level-1 single-look complex (SLC) images were obtained from the Alaska Satellite Facility (ASF) data portal (https://search.asf.alaska.edu/ (accessed on 20 October 2026)). Four Interferometric Wide Swath (IW), VV-polarized stacks, comprising two ascending and two descending tracks, cover the regional survey domain. The acquisition periods, image counts, and imaging-geometry fields are summarized in Table 1; the four stacks contain 797 images in total.

The incidence and heading angles summarized in Table 1 are acquisition-metadata values extracted from the corresponding SLC parameter files. The APF inversion used pixel-specific LOS geometry, as described in Section 3.1. Incidence is measured from the local vertical, and heading is measured clockwise from north; negative heading values denote angles west of north. Path 128/Frame 114 and Path 135/Frame 473 provide the ascending and descending observations for the Li-Kan Highway landslide.

For the Li-Kan Highway landslide, the nominal overlap between the ascending Path 128/Frame 114 stack and the descending Path 135/Frame 473 stack is 27 March 2018 to 9 October 2024. This overlap does not imply coincident acquisition dates. The actual three-dimensional reconstruction period was 27 March 2018 to 6 May 2024. The output

list comprises 322 epoch entries on 183 distinct calendar dates. The common grid, joint temporal formulation, and common reference are described in Section 3.1.

Table 1. Sentinel-1A acquisition metadata for the regional survey and case study.

Orbit	Path/Frame	Acquisition Period	Images	Incidence (°)	Heading (°)
Ascending	128/114	20 March 2017–9 October 2024	195	39.15	−13.10
Ascending	26/113	13 March 2017–2 October 2024	173	41.55	−13.12
Descending	33/472	18 January 2016–30 January 2025	243	39.98	193.09
Descending	135/473	27 March 2018–25 January 2025	186	43.83	193.06

The auxiliary datasets used in this study are summarized in Table 2. The external elevation dataset was the Copernicus digital elevation model (Copernicus DEM), with an original spatial resolution of 30 m. It was used for topographic-phase removal in InSAR processing and to provide the terrain information for the case study. The original DEM resolution is distinguished from any resampled analysis or simulation grid.

Table 2. Auxiliary datasets for the Li-Kan Highway landslide case study.

Data	Product or Provider	Resolution	Coverage and Use
Elevation	Copernicus DEM	30 m	Topographic-phase removal and case-study terrain information.
Rainfall	GPM IMERG 3.7	0.1° × 0.1°; daily	1 January 2015–31 December 2024; nearest grid center: 101.75°E, 36.15°N; aggregated to 12 d totals.
Optical basemap	Google Earth	Export: 0.482462 m/pixel	September 2022; WGS 1984; 6400 × 5632 pixels; no additional image preprocessing; used in the potential failure analysis (Section 5.3).

Daily rainfall was obtained from the Global Precipitation Measurement (GPM) Integrated Multi-satellitE Retrievals for GPM (IMERG) 3.7 product, with a nominal grid spacing of 0.1° × 0.1°. The record used in this study spans 1 January 2015 to 31 December 2024. Among the grid cells covering the study area, the cell whose center was closest to the Li-Kan Highway landslide was selected. Its center is located at 101.75°E, 36.15°N, approximately 5 km from the landslide, and its daily series was used as a grid-scale proxy for rainfall near the site. Daily amounts were summed into 12 d accumulations and assigned to the interval-ending dates for alignment with deformation, as described in Section 3.3.

The optical basemaps used in this study were obtained from Google Earth Pro (version 7.3.6; Google LLC, Mountain View, CA, USA) and acquired in September 2022. The exported raster has 6400 × 5632 pixels in the WGS 1984 geographic coordinate system and covers 101.781463623–101.815795898°E and 36.091461182–36.121673584°N. The reported export pixel size is 0.482462 m/pixel (approximately 0.48 m). The imagery was downloaded directly and used for qualitative interpretation without additional image preprocessing.

A continuous Lijiaxia Reservoir water-level record covering the InSAR observation period was not available for this study. The 2180 m normal water level in Figure 1 is a reference elevation rather than a time-varying forcing series. Potential reservoir-level effects and the resulting attribution limits are discussed in Section 5.3.

3. Methodology

Figure 3 presents the technical workflow of this study, comprising InSAR processing and four core spatiotemporal analyses. Ascending- and descending-track Sentinel-1 single-look complex images and an external DEM were used to generate differential interferograms and coherence products; phase unwrapping and atmospheric correction were then performed to derive LOS deformation velocities and time series. These products provide the regional deformation context and the observations required for detailed analysis of the Li-Kan Highway landslide.

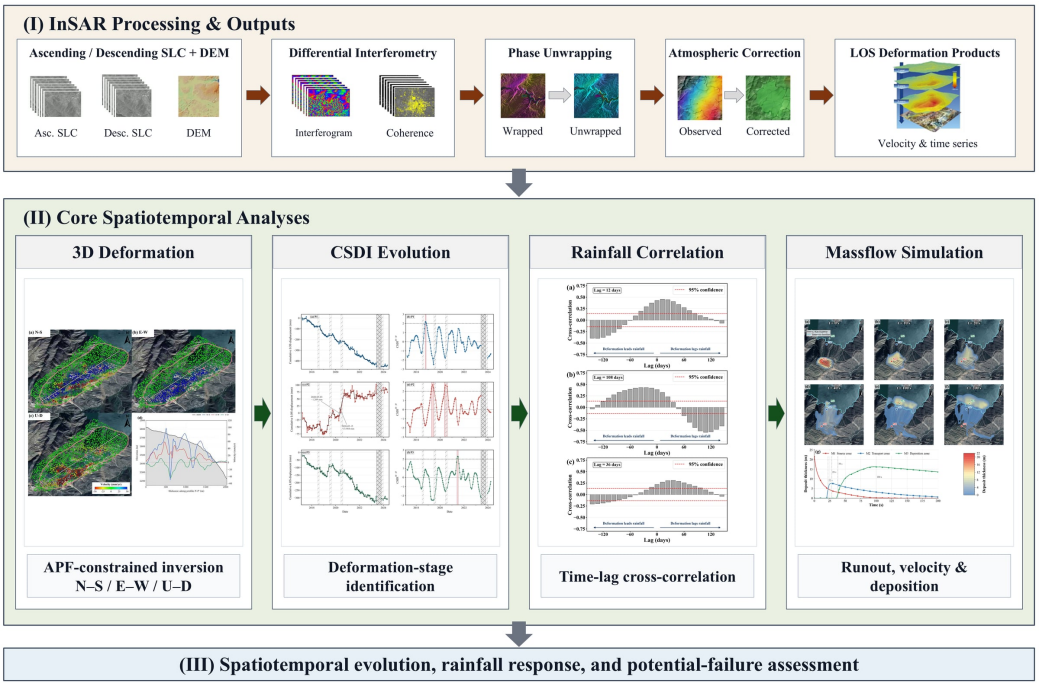


Figure 3. Technical workflow of InSAR processing and core spatiotemporal analyses for the Li-Kan Highway landslide.

For the case study, ascending- and descending-track LOS observations were integrated through aspect-parallel-flow-constrained inversion to reconstruct the north–south, east–west, and vertical deformation components. The CSDI was subsequently used to identify deformation stages, and time-lag cross-correlation was applied to quantify the delayed response of deformation to rainfall. Finally, the inferred source area and deformation characteristics were used to constrain Massflow simulations of runout, velocity, and deposition, thereby linking deformation monitoring, spatiotemporal evolution, rainfall response, and potential-failure assessment.

3.1. Three-Dimensional InSAR Deformation Reconstruction

The ascending- and descending-track Sentinel-1 stacks were processed separately using GAMMA software (2018 release; GAMMA Remote Sensing AG, Gümligen, Switzerland) for SAR image co-registration, differential interferogram generation, filtering, and phase unwrapping. Each acquisition was paired with the next four available acquisitions in chronological order, subject to a perpendicular baseline threshold of 150 m. Before phase

unwrapping, a threshold of 0.4 on mean coherence was applied to mask low-quality pixels. Topographic phase was removed using the 30 m Copernicus DEM described in Section 2.2. After atmospheric correction, the two orbit sets of interferogram displacement maps were jointly inverted using MSBAS software (version 10; Canada Centre for Mapping and Earth Observation, Natural Resources Canada, Ottawa, ON, Canada) with the APF constraint. For the case study, the reference point was selected on the rooftop of a stable building in Kanbula Town (101.835°E, 36.115°N), approximately 3 km northeast of the landslide. The point had a mean coherence greater than 0.95 over the Sentinel-1 observation period, and no obvious persistent deformation was observed in its surroundings. Both orbit datasets were referenced to this same ground location before the joint inversion.

The original ascending-track stack (Path 128/Frame 114) spans 20 March 2017 to 9 October 2024, whereas the descending-track stack (Path 135/Frame 473) spans 27 March 2018 to 25 January 2025. Their nominal temporal overlap is therefore 27 March 2018 to 9 October 2024. The ascending- and descending-track interferogram displacement maps were combined on a common WGS 84 geographic grid (EPSG:4326), with a spacing of 0.5 arc-second in longitude and latitude. No additional spatial resampling was performed when combining the two tracks. Their pixel-dependent LOS projection coefficients and the APF constraint were used to jointly solve for the common north, east, and up components.

Temporal matching was performed through the joint MSBAS time-interval matrix. Each interferogram constrains the accumulated displacement over the time intervals between its acquisitions, with interval velocities weighted by their durations [48]. The common output period was 27 March 2018 to 6 May 2024, and the output list contains 322 epoch entries on 183 distinct calendar dates. The first output epoch, 27 March 2018, was used as the common displacement reference date. The 12 d sequence used for wavelet analysis was prepared separately from the point time series, as described in Section 3.3.

Small localized missing-data patches in the input displacement maps were filled using inverse-distance-weighted (IDW) interpolation. Pixels with excessive missing observations were excluded based on the number of missing values at the same pixel across all ascending- and descending-track interferograms. The remaining valid observations were used in the inversion. Interferograms lying wholly outside the common analysis period were excluded. For interferograms crossing an analysis boundary, the displacement constraint was scaled by the fraction of the original pair duration retained within the analysis period. This proportional adjustment uses the pair-averaged LOS velocity to approximate displacement over the retained interval.

Ascending- and descending-track InSAR observations provide two LOS constraints and therefore cannot independently determine all three geographic deformation components. The near-polar orbit geometry also provides limited sensitivity to north–south motion [49]. We therefore introduce the aspect-parallel flow (APF) constraint, which relates the horizontal deformation components through the local slope aspect [50,51]. The APF-constrained reconstruction was implemented using MSBAS Software Version 10 [48]. APF provides a kinematic constraint rather than a third independent SAR observation, so the reconstructed components must be interpreted under the assumption of negligible cross-slope motion.

Figure 4 shows the ascending and descending viewing geometries and the global geographic and local slope coordinate systems. The geographic frame comprises east (E), north (N), and up (U). O denotes the coordinate origin in each schematic. The LOS arrows in Figure 4a point from the ground toward the respective satellites. The geometry is schematic and is not drawn to scale. The reconstruction used pixel-specific viewing and terrain angles; incidence and heading defined the LOS projection coefficients for both orbits. The scalar entries in Table 1 summarize acquisition metadata from the SLC parameter files. Incidence is measured from the local vertical, and heading is measured clockwise from north, with

negative values denoting angles west of north. Positive LOS displacement denotes ground motion toward the satellite, and negative LOS displacement denotes motion away from the satellite.

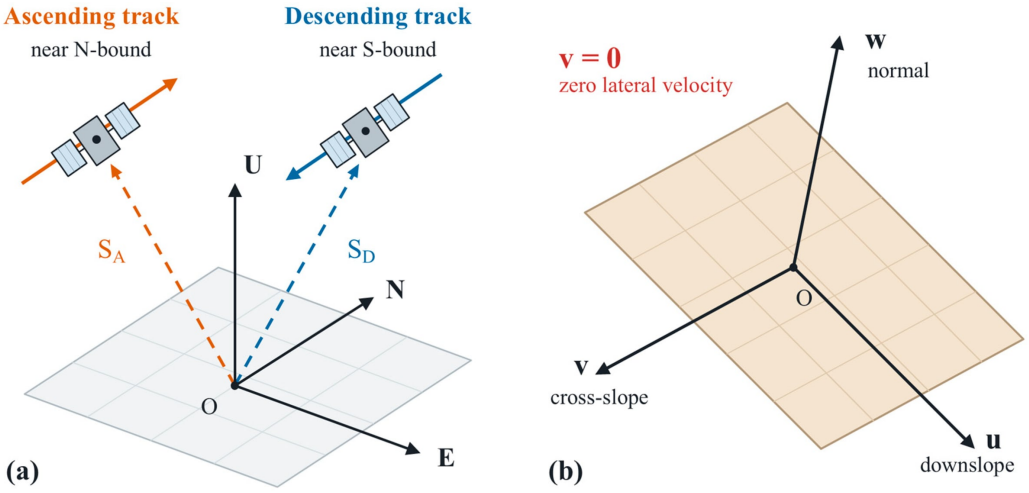


Figure 4. Geometry of APF-constrained three-dimensional deformation reconstruction: (**a**) ascending- and descending-track InSAR viewing geometries; (**b**) local slope coordinate system and the APF constraint.

In the local slope coordinate system, the u axis points along the maximum downslope direction; the w axis is normal to the slope surface; and the v axis lies within the slope surface and is orthogonal to the u axis. The velocity component within the slope-parallel plane and perpendicular to the aspect direction is assumed to be zero, i.e., $v = V_N \sin\beta - V_E \cos\beta = 0$ [51]. This constraint makes the horizontal motion collinear with the slope-aspect axis while allowing a nonzero slope-normal component; it does not require the full three-dimensional velocity to be parallel to the slope surface [50]. The resulting constrained inversion is:

$$\begin{bmatrix} V_{L-S1A} \\ V_{L-S1D} \\ v \end{bmatrix} = \begin{bmatrix} S_{S1A} \\ S_{S1D} \\ S_v \end{bmatrix} \begin{bmatrix} V_N \\ V_E \\ V_U \end{bmatrix} \quad (1)$$

where V_{L-S1A} and V_{L-S1D} are the LOS deformation rates obtained from ascending- and descending-track Sentinel-1 observations, respectively; S_{S1A} and S_{S1D} are the unit LOS observation vectors for the ascending and descending tracks, respectively; and $S_v = [\sin\beta \; -\cos\beta \; 0]$ is the unit vector along the v direction of the local landslide coordinate system. The geographic components in Equation (1) are ordered north, east, and up. Equation (1) summarizes the LOS projection relations and APF constraint for interval velocities. The MSBAS time-series inversion combines these geometric relations with the interferogram time intervals and jointly solves the interval velocities [48].

The reconstructed geographic components are then rotated into the local slope coordinate system using:

$$\begin{bmatrix} u \\ w \\ v \end{bmatrix} = \begin{bmatrix} \cos\sigma\cos\beta & \cos\sigma\sin\beta & -\sin\sigma \\ \sin\sigma\cos\beta & \sin\sigma\sin\beta & \cos\sigma \\ \sin\beta & -\cos\beta & 0 \end{bmatrix} \begin{bmatrix} V_N \\ V_E \\ V_U \end{bmatrix} \quad (2)$$

where σ is the slope angle measured from the horizontal and β is the slope aspect measured clockwise from north. The local components in Equation (2) are ordered u, w, and v.

3.2. Identification of Deformation Evolution Stages from InSAR Time Series

To characterize changes in the movement state of the Li-Kan Highway landslide during long-term deformation, three representative InSAR monitoring points (P1, P2, and P3) at different slope locations were selected for time-series analysis. Preliminary sensitivity analysis showed that the ascending-track geometry is more sensitive to aspect-parallel motion of this landslide than the descending-track geometry. The ascending InSAR time series was therefore used as the primary dataset for deformation-stage analysis, while descending-track results were used for supplementary interpretation. Sentinel-1 acquisitions are not strictly equally spaced in time and contain several data gaps; directly differencing adjacent displacement observations can therefore amplify short-period fluctuations. To adapt the CSDI velocity input to irregular InSAR sampling, each cumulative LOS displacement series was first aligned with its dominant long-term deformation direction (direction factors: −1 for P1, +1 for P2, and −1 for P3), and tricube-weighted local linear regression was applied using the actual SAR acquisition dates. The resulting local LOS velocities retained their signs; no absolute-value transformation was applied, thereby preserving information on local deceleration and motion opposite to the dominant direction. The direction factors were used only to construct the CSDI input; the physical LOS displacement sign convention in Section 3.1 remains unchanged. For a target time t_i, the cumulative LOS displacement within the local window is expressed as:

$$D(t_j) = a_0 + a_1\left(t_j - t_i\right) + \varepsilon_j \tag{3}$$

The local deformation velocity at the target time is then:

$$V(t_i) = a_1 \tag{4}$$

where $D(t_j)$ is the cumulative LOS displacement at time t_j, and a_0 and a_1 are the local intercept and deformation-rate parameters, respectively. A local regression half-window of 120 d (observations within ±120 d of each target acquisition date) was used as the primary setting, with 96 d and 144 d half-windows used for sensitivity analysis. Observation intervals of 37–60 d were flagged as low-confidence gaps, whereas intervals longer than 60 d were treated as hard gaps; velocity was not estimated across hard gaps. The 37 d lower bound denotes an interval longer than three nominal 12 d observation cycles (36 d); this is an operational data-quality flag, not a physical threshold for landslide activity. The Comprehensive Standardized Deformation Index (CSDI) was then applied to characterize relative changes in deformation activity over time. The index identifies statistical deformation-activity stages from the distribution of local LOS velocity. In this study, stage classification uses $CSDI^{M-M}$ constructed from $Min - Max$ normalization. The local deformation velocity is first normalized using $Min - Max$:

$$V_i^{M-M} = \frac{V_i - V_{\min}}{V_{\max} - V_{\min}} \tag{5}$$

where $V_{\max}$ and $V_{\min}$ are the maximum and minimum values of the velocity series, respectively. Let M denote the number of non-positive velocity samples after Min–Max normalization, and N denote the total number of valid normalized velocity samples; the corresponding probability is:

$$P = \frac{M}{N} \tag{6}$$

Five candidate probability distributions (Gamma, lognormal, log-logistic, logistic, and Weibull) were fitted to the positive part of the Min–Max-normalized velocity series. The best-fitting cumulative distribution function $F(v)$ was selected by maximizing the coefficient of determination (R^2) between the empirical and fitted theoretical cumulative distribution

functions. For the primary 120 d half-window, Logistic was optimal for P1, P2, and P3, with R^2 values of 0.998, 0.988, and 0.977, respectively. The complete cumulative distribution was constructed as:

$$G(v) = P + (1 - P)F(v) \tag{7}$$

An equal-cumulative-probability transformation is subsequently applied to map the distribution into standard-normal space:

$$CSDI_i^{M-M} = \Phi^{-1}[G(V_i)] \tag{8}$$

where $\Phi^{-1}(\cdot)$ is the inverse cumulative distribution function of the standard normal distribution and $CSDI^{M-M}$ is a dimensionless continuous index describing the statistical state of the deformation velocity at each time. According to the CSDI stage-classification criterion, $CSDI^{M-M} < 0$ corresponds to Stage II (uniform deformation stage), representing relatively uniform and persistent deformation; $0 \leq CSDI^{M-M} < 2$ corresponds to Stage I (initial deformation stage), representing initial deformation or adjustment of the movement state; and $CSDI^{M-M} \geq 2$ corresponds to Stage III (accelerated deformation stage), indicating deformation activity that is clearly enhanced relative to the long-term statistical background. Thus, 0 and 2 are used as boundaries between the statistical movement stages. These CSDI-defined Stage I–III categories are kinematic statistical states and should not be interpreted directly as stable, pre-failure, or overall-failure states. Because the Li-Kan Highway landslide did not undergo overall failure during the study period, locally identified Stage III intervals are interpreted as statistically enhanced deformation activity rather than as direct failure criteria. Final stage identification is not based on isolated CSDI peaks; instead, it jointly considers the persistence of CSDI changes, the original LOS displacement trend, observation gaps, and consistency among the 96 d, 120 d, and 144 d half-windows. An active interval is treated as meaningful evidence of a local kinematic adjustment only when it is repeatedly identified across multiple windows and is supported by the original InSAR time-series behavior. This procedure reduces the influence of short-period fluctuations and irregular temporal sampling while retaining persistent deformation signals.

3.3. Continuous Wavelet Transform

Ascending-track LOS displacement time series were extracted at P1–P3 and resampled to a regular 12 d grid. The ascending track was selected because it provided greater sensitivity to downslope motion than the descending track in this case study. Observations coinciding with target dates were retained; values at other dates were estimated by linear interpolation between the nearest preceding and following observations. At the record boundaries, the nearest available observation was used where necessary.

The resampled series were separated into trend, seasonal, and remainder components using seasonal-trend decomposition based on LOESS (STL) [52,53]. Considering annual environmental forcing such as rainfall and freeze–thaw cycles and the 12 d Sentinel-1 revisit interval, the seasonal period was set to 30 observation samples, corresponding to approximately 360 d (nearly 1 year), to match annual seasonal variability. The seasonal components were used as the deformation inputs to CWT and TLCC in Section 5.2.

Daily rainfall was summed over each corresponding 12 d interval and assigned to its ending date to align it with the deformation grid. The daily GPM rainfall record had no missing values. The Morlet wavelet was applied to the seasonal components and the matched rainfall series.

The Continuous Wavelet Transform (CWT) uses a variable time–frequency window and adaptively balances temporal and frequency resolution, allowing features at different

scales and local temporal variations to be captured effectively [54]. For a signal $f(t)$, the CWT is defined as:

$$W_f(s,\tau) = \frac{1}{\sqrt{s}}\int_{-\infty}^{+\infty} f(t)\cdot\psi^*\left(\frac{t-\tau}{s}\right)dt = \left\langle f(t), \psi_{s,\tau}(t)\right\rangle \quad (9)$$

where s is the scale factor, τ is the translation parameter, and ψ^* denotes the complex conjugate of the basis function ψ.

The Morlet wavelet basis function is:

$$\psi(t) = \frac{1}{\sqrt[4]{\pi}} e^{-\frac{t^2}{2}}\left(e^{i\omega_0 t} - e^{-\frac{\omega_0^2}{2}}\right) \quad (10)$$

where ω_0 is the dimensionless central frequency controlling the number of wavelet oscillations; it was set to 6 in this study.

The continuous wavelet transform is formulated for continuous signals. In practical applications, however, the signal and basis function must be discretized to reduce computational complexity and redundancy. This procedure is referred to as the discrete form or discrete approximation of the continuous wavelet transform [55].

For a discrete signal $x(m)$, the basic wavelet-transform form is:

$$W_n(s) = \sqrt{\frac{\Delta t}{s}}\sum_{m=0}^{N-1} x(m)\cdot\psi^*\left[\frac{(m-n)\Delta t}{s}\right] \quad (11)$$

3.4. Time-Lag Cross-Correlation Analysis

Time-lag cross-correlation (TLCC) evaluates the correlation between two time series under different temporal offsets. For two series $ts1$ (deformation) and $ts2$ (rainfall), the series should have the same length. The lag order is the relative shift between the two series along the time axis and is expressed in units of the sampling interval. Correlation coefficients are calculated for different lag orders, and the lag corresponding to the maximum absolute correlation coefficient is used to characterize the temporal offset between the two series. When the lag order is 1 ($offset = 1$), $ts2$ is shifted forward by one sampling interval to produce $ts2-1$. To align with the shifted $ts2$, $ts1$ is truncated to the same length as $ts2-1$, producing $ts1-1$, and the correlation coefficient k between $ts1-1$ and $ts2-1$ is then calculated. Repeating this procedure for different lag orders yields the lag-dependent relationship between the two time series [56].

For TLCC, the deformation input was the STL-derived seasonal component of the ascending-track LOS displacement series at each monitoring point, rather than the original cumulative LOS displacement. Under the null hypothesis of zero cross-correlation and a large-sample white-noise approximation, the standard error of the sample cross-correlation coefficient is approximately $1/\sqrt{N}$. The two-sided 95% confidence bounds were calculated as $\pm 1.96/\sqrt{N}$, where 1.96 is the 97.5th percentile of the standard normal distribution and N denotes the number of paired observations in the aligned rainfall and deformation series for each monitoring point. For each point, the same full-series sample size was used across all evaluated lags, resulting in fixed horizontal significance bounds for the lag-correlation analysis. These are approximate pointwise bounds for individual lag correlations, rather than confidence intervals for the estimated lag times. The red dashed lines indicate approximate pointwise significance bounds; correlation coefficients outside these bounds are statistically significant at the 95% level under the stated approximation.

3.5. Numerical Simulation of Potential Failure

To evaluate the post-failure dynamics and potential impact area of the Li-Kan Highway landslide, the Massflow numerical model (version 2.0; Institute of Mountain Hazards and

Environment, Chinese Academy of Sciences, Chengdu, China) was used to simulate the complete process from release through rapid runout to final deposition. Massflow is based on depth-integrated continuum theory and treats the moving mass as a continuum flowing over complex terrain. Under the assumptions of hydrostatic pressure distribution and a kinematic free-surface boundary condition, the three-dimensional Navier–Stokes equations are integrated vertically and reduced to two-dimensional depth-averaged mass and momentum conservation equations [57]. This approach retains the main dynamic characteristics while substantially improving computational efficiency for large-scale landslide runout simulation [39,58,59]. The mass-conservation equation is:

$$\frac{\partial h}{\partial t} + \frac{\partial (hu)}{\partial x} + \frac{\partial (hv)}{\partial y} = 0 \tag{12}$$

The momentum-conservation equations in the two horizontal directions are:

$$\frac{\partial (hu)}{\partial t} + \frac{\partial \left(hu^2 + \frac{k_{ap} g h^2}{2} \right)}{\partial x} + \frac{\partial (huv)}{\partial y} = -k_{ap} g h \frac{\partial z_b}{\partial x} - \frac{(\tau_{zx})_b}{\rho} \tag{13}$$

$$\frac{\partial (hv)}{\partial t} + \frac{\partial (huv)}{\partial x} + \frac{\partial \left(hv^2 + \frac{k_{ap} g h^2}{2} \right)}{\partial y} = -k_{ap} g h \frac{\partial z_b}{\partial y} - \frac{(\tau_{zy})_b}{\rho} \tag{14}$$

where h is the landslide thickness; u and v are the depth-averaged velocities in the x and y directions, respectively; ρ is the density of the moving mass; g is gravitational acceleration; z_b is the basal topographic elevation; $(\tau_{zx})_b$ and $(\tau_{zy})_b$ are the basal-resistance components in the x and y directions, respectively; and k_{ap} is the lateral earth-pressure coefficient. These equations describe the balance among mass conservation, gravitational forcing due to terrain, momentum transport, and basal resistance. Because the Li-Kan Highway landslide is expected to shear mainly along the loess–mudstone interface, a Coulomb friction model is adopted to describe the mechanical interaction between the moving mass and the basal surface. In Massflow, basal shear stress satisfies the Coulomb failure criterion:

$$\tau_b = c + \rho\, g h\, \tan\, \delta \tag{15}$$

where τ_b is the basal shear stress, c is the cohesion of the sliding material, and δ is the basal friction angle between the moving mass and the bed, which primarily controls basal frictional resistance during motion.

The mass and momentum conservation equations are solved using a MacCormack–TVD finite-difference scheme [39]. Massflow also employs a variable time step controlled by the Courant condition and can improve computational efficiency through grid optimization and MPI/OpenMP parallelization.

The numerical model of the Li-Kan Highway landslide was constructed from the terrain, the prescribed potential release area, an initial thickness field and material parameters. The simulations were performed using Massflow V2.0. The terrain was represented by a regular grid with 300 columns and 330 rows at a spacing of 7 m in both horizontal directions, covering 2100 m × 2310 m. This computational spacing is distinguished from the 30 m original DEM resolution reported in Section 2.2.

The potential source area was delineated by jointly considering the three-dimensional InSAR deformation pattern, CSDI-defined deformation activity, surface cracks and the mapped landslide boundary. The prescribed release area represents a potential post-failure scenario rather than the whole mapped landslide. A spatially variable initial thickness field was generated within the Massflow modeling workflow using empirical source-area–volume relationships, with greater thickness near the rear scarp and progressive thinning downslope. Published thickness estimates for the same landslide [16] were used as external

geometric references. The resulting release field had an area of approximately 11.84×10^4 m^2, a volume of approximately 1.26×10^6 m^3, a mean thickness of 10.60 m and a maximum thickness of 21.44 m.

The principal physical and mechanical parameters include density ρ, cohesion c, internal friction angle ϕ, and basal friction angle δ. Table 3 summarizes the adopted physical and mechanical parameter values and units. Density and internal friction angle were selected with reference to Zhao et al. [60], who reported a natural density of 1650 kg/m^3 and an internal friction angle of 26.29°. A scenario density of 1800 kg/m^3 was adopted. The basal friction coefficient μ was 0.40, within the published reference range of 0.25–0.40 [60], and corresponds to a basal friction angle δ of approximately 21.80°. Cohesion was set to 7 kPa, an approximate rounded value near the lower end of the reported 7.24–8.15 kPa range [44]. The excess pore-water pressure coefficient λ was zero, so no additional pore-pressure-induced reduction in basal friction was applied.

Table 3. Physical and mechanical parameters adopted in the Massflow simulation.

Parameter	Symbol	Value	Unit
Density	ρ	1800	kg/m^3
Cohesion	c	7	kPa
Internal friction angle	ϕ	26.29	°
Basal friction angle	δ	21.80	°
Excess pore-water pressure coefficient	λ	0	-

The prescribed source mass was released simultaneously from rest at the beginning of the simulation, and subsequent motion developed under gravity. Wall boundary conditions were applied at all four outer boundaries of the computational domain, preventing material from crossing those boundaries. The computations used the MacCormack–TVD finite-difference scheme [39] and a Courant-controlled variable time step.

For the prescribed source geometry and material parameters, the model calculates flow thickness, velocity and spatial extent at successive time steps. These outputs characterize potential acceleration, runout and deposition.

4. Results

4.1. Three-Dimensional InSAR Deformation of the Li-Kan Highway Landslide

As shown in Figure 5a–c, the horizontal movement of the Li-Kan Highway landslide is predominantly northeastward, reflecting the main gravity-driven movement direction. Local differences in the north–south and east–west components, including southward motion in part of the slope, indicate contrasting movement directions among slope sectors. These variations suggest that the landslide may comprise multiple kinematic units with complex internal deformation rather than a uniformly moving block. Figure 5d further relates the deformation pattern to elevation. A profile P–P′ was drawn from the rear of the slope toward the toe along the principal sliding direction, and the corresponding north–south (NS), east–west (EW), and vertical (UD) deformation velocities derived from the APF-constrained three-dimensional InSAR inversion were extracted along the profile. The P–P′ profile extends approximately 2 km; its horizontal length was calculated from the verified endpoints in WGS 84/UTM Zone 47N (EPSG:32647). DEM elevation is displayed along the same transect. The three-dimensional deformation rates show clear spatial variations, including local changes in velocity magnitude and a sign change in the NS component, indicating heterogeneous deformation along the slope.

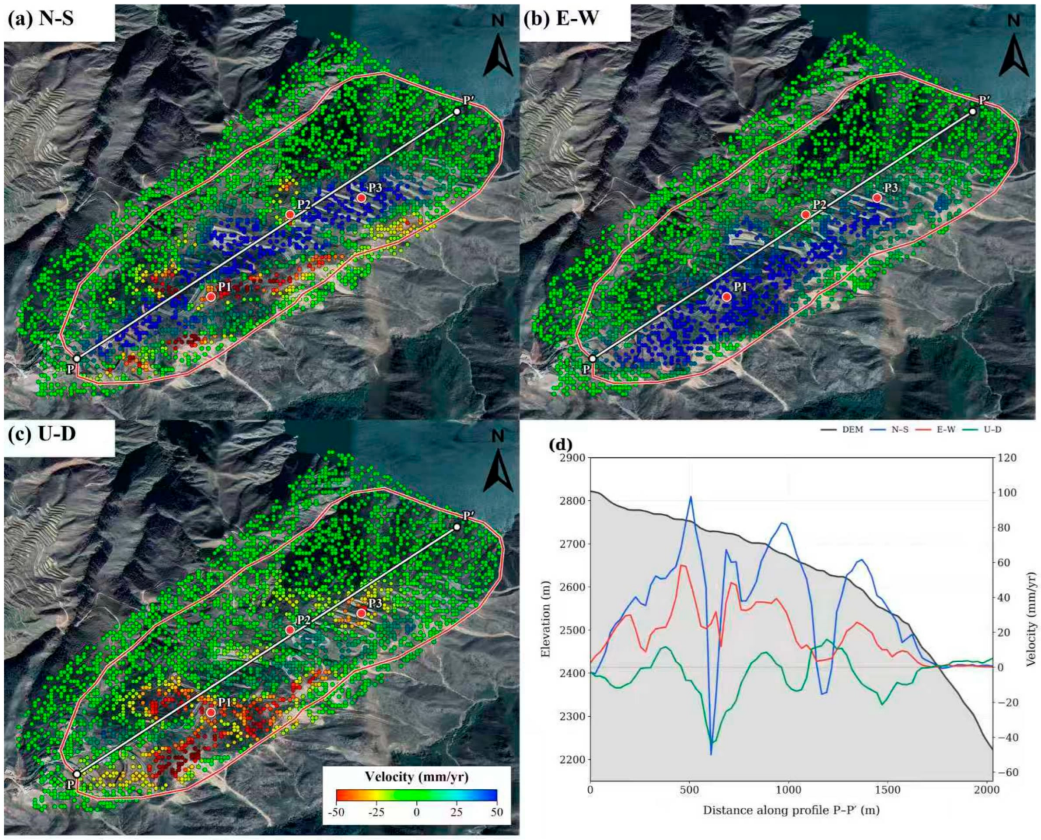


Figure 5. APF-constrained three-dimensional InSAR deformation velocities of the Li-Kan Highway landslide: (**a**) north–south (NS), (**b**) east–west (EW), and (**c**) vertical (UD) components; (**d**) corresponding velocity profiles and DEM elevation along P–P′. Panels (**a**–**c**) share a velocity color scale and show the same P–P′ transect and the interpreted landslide boundary (red outline). P1–P3 indicate the representative InSAR monitoring points used for time-series analysis. Positive NS, EW, and UD velocities denote northward, eastward, and upward motion, respectively; negative values denote southward, westward, and downward motion.

4.2. PCA-Based Analysis of Three-Dimensional Deformation Patterns

Three-dimensional landslide deformation can reflect the combined effects of gravity-driven sliding, local uplift, lateral extension, and other processes. Principal Component Analysis (PCA) decomposes mixed signals into mutually uncorrelated principal components, each representing a dominant mode of variability. The main procedure includes: (1) centering the data; (2) calculating the covariance matrix; (3) calculating eigenvalues and eigenvectors; and (4) selecting and projecting the principal components. In this study, however, PCA is applied to the three-dimensional deformation components. PCA identifies orthogonal directions of maximum variance and ranks them by explained variance; it is determined only by data covariance. The principal-component directions therefore represent the main axes of data dispersion and do not necessarily correspond to physical movement directions. Nevertheless, spatial score maps of the principal components can be used to identify anomalous zones. Accordingly, PCA is used here to characterize deformation variability, not to estimate InSAR measurement error or independently validate reconstruction accuracy.

As shown in Figure 6a, PC1 and PC2 together explain 85.6% of the variance and provide a compact description of the deformation variability. This explained-variance percentage is not a measure of InSAR accuracy. Figure 6b shows the component loadings, which describe the correlations between the original variables and the principal components. Their magnitudes indicate the contributions of the original variables, whereas their signs

indicate the directions of correlation. The absolute EW and UD loadings are high for PC1, indicating that PC1 mainly reflects the relationship between east–west and vertical motion. For PC2, the NS loading is much larger than the EW and UD loadings, indicating that PC2 mainly represents north–south motion. Spatial score maps of PC1 and PC2 are shown in Figure 7. The results suggest that a secondary landslide may exist on the left side of the main landslide.

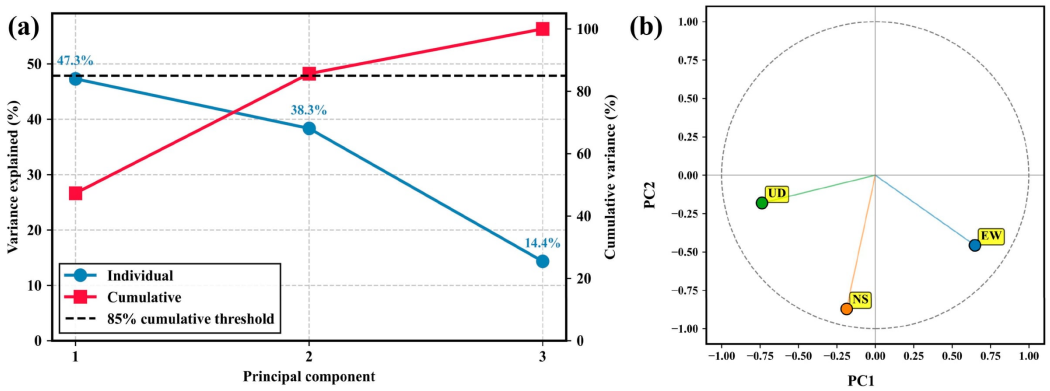


Figure 6. PCA results: (**a**) cumulative explained variance; (**b**) loadings of PC1 and PC2.

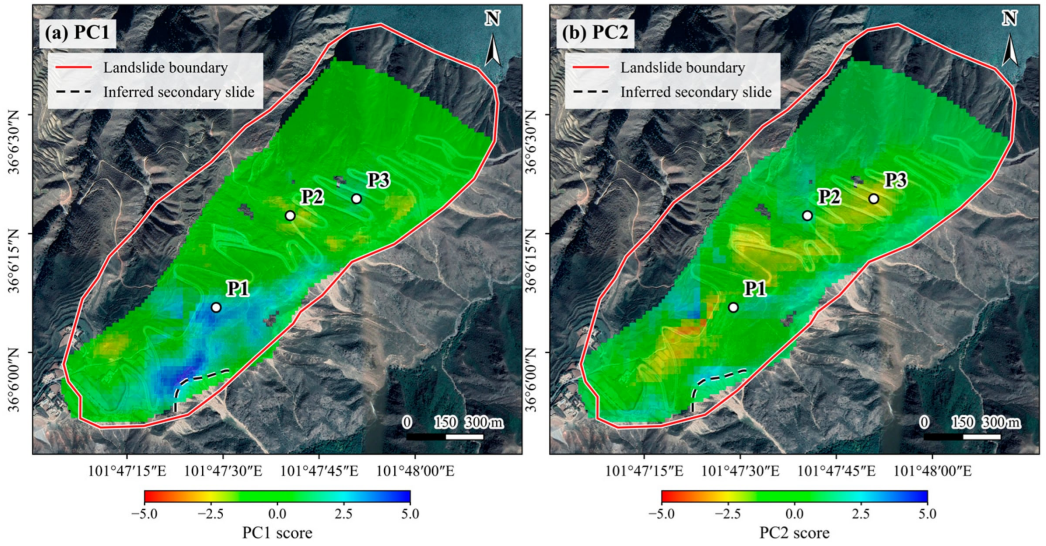


Figure 7. Spatial score maps of (**a**) PC1 and (**b**) PC2 overlaid on optical imagery, showing the locations of monitoring points P1–P3. Red solid lines indicate the mapped landslide boundary, and black dashed lines mark the boundary of the inferred secondary sliding body.

Figure 7 overlays the PC1 and PC2 spatial scores on optical imagery and marks the geographic locations of P1–P3. Red solid lines show the mapped landslide boundary, whereas black dashed lines delimit the inferred secondary sliding body. This secondary boundary is interpretive rather than an independently confirmed geological contact. Profile P–P′ remains in Figure 5, where it supports the deformation–velocity and elevation analysis.

The three-dimensional displacement time series extracted at P1-P3 are shown in Figure 8. At P2, both north–south (NS) and vertical (UD) displacements are pronounced. After January 2021, the absolute cumulative NS displacement is generally greater than the UD and east–west (EW) components (Figure 8b). In contrast, vertical displacement at P1 and P3 is smaller than the horizontal components, indicating predominantly horizontal deformation at these two locations. This behavior may be related to a relatively shallow sliding surface.

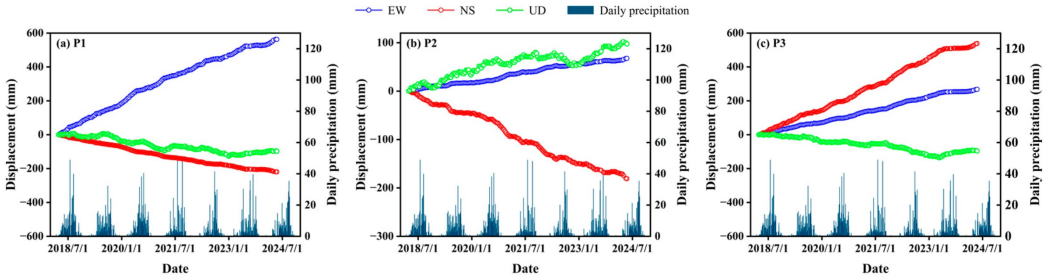


Figure 8. Three-dimensional cumulative displacement time series and daily precipitation at representative monitoring points: (**a**) P1; (**b**) P2; (**c**) P3. Blue, red, and green curves represent the east–west (EW), north–south (NS), and vertical (UD) displacement components, respectively, referenced to the left axis. Dark-blue bars show daily precipitation, referenced to the right axis. These are reconstructed geographic displacement components, not LOS displacement. Positive NS, EW, and UD displacements denote northward, eastward, and upward motion, respectively; negative values denote southward, westward, and downward motion.

5. Discussion

5.1. Deformation Evolution of the Li-Kan Highway Landslide

The Li-Kan Highway landslide shows persistent deformation throughout the InSAR observation period. Ascending- and descending-track SBAS-InSAR results indicate maximum LOS deformation rates of approximately −93 mm/yr and 92 mm/yr, respectively, with the main deforming area showing an overall tongue-shaped pattern. The corresponding ascending-track LOS and CSDI time series are shown in Figure 9. The CSDI results indicate that periods of enhanced deformation activity at the InSAR monitoring points P1, P2, and P3 are not synchronous. Enhanced activity at P1 occurs mainly in autumn 2018; P2 shows pronounced responses from spring to early summer 2019 and again in spring–summer 2020; P3 shows a local increase around mid-2021, but its persistence across different analysis windows is weaker than that of P1 and P2.

The CSDI panels of Figure 9 share a common −3 to 3 vertical scale, whereas the LOS displacement panels retain point-specific ranges to preserve smaller variations. For the primary 120 d half-window, Stage III observations span 5–29 October 2018 at P1; 15 April–26 June 2019 and 15 May–7 August 2020 at P2; and 3 June–9 July 2021 at P3. These intervals connect qualifying SAR acquisitions rather than continuous daily observations. Across the 96, 120, and 144 d half-windows, P3 has only one jointly supported Stage III acquisition (15 June 2021).

The marked timing offsets among the three points indicate that the Li-Kan Highway landslide does not evolve synchronously as a single block but instead shows strong temporal asynchrony. A marked change is observed at P2 in spring 2020. In the original ascending-track series, P2 changes from −1.209 mm on 3 May 2020 to +15.984 mm on 15 May 2020, so the cumulative LOS displacement crosses zero between two consecutive observations; this zero crossing alone does not establish a reversal of the physical movement direction. The CSDI indicates a statistically high-activity interval around this period. Considering the spatial deformation results in Section 4.1 together with the monitoring-point displacement time series in Section 4.2 (Figure 8), the movement components differ substantially among slope sectors: horizontal motion is predominantly northeastward, P2 exhibits notable north–south and vertical displacement components, and P1 and P3 are dominated by horizontal motion. As shown in Figure 8b, the absolute cumulative NS displacement at P2 is generally greater than the UD and EW components after January 2021. Taken together, these observations are consistent with local kinematic adjustment at P2, rather than demonstrating synchronous acceleration of the entire landslide. The 60 d acquisition gap from 8 June to

7 August 2020 is classified as low-confidence; uninterrupted acceleration throughout this Stage III observation span therefore cannot be inferred.

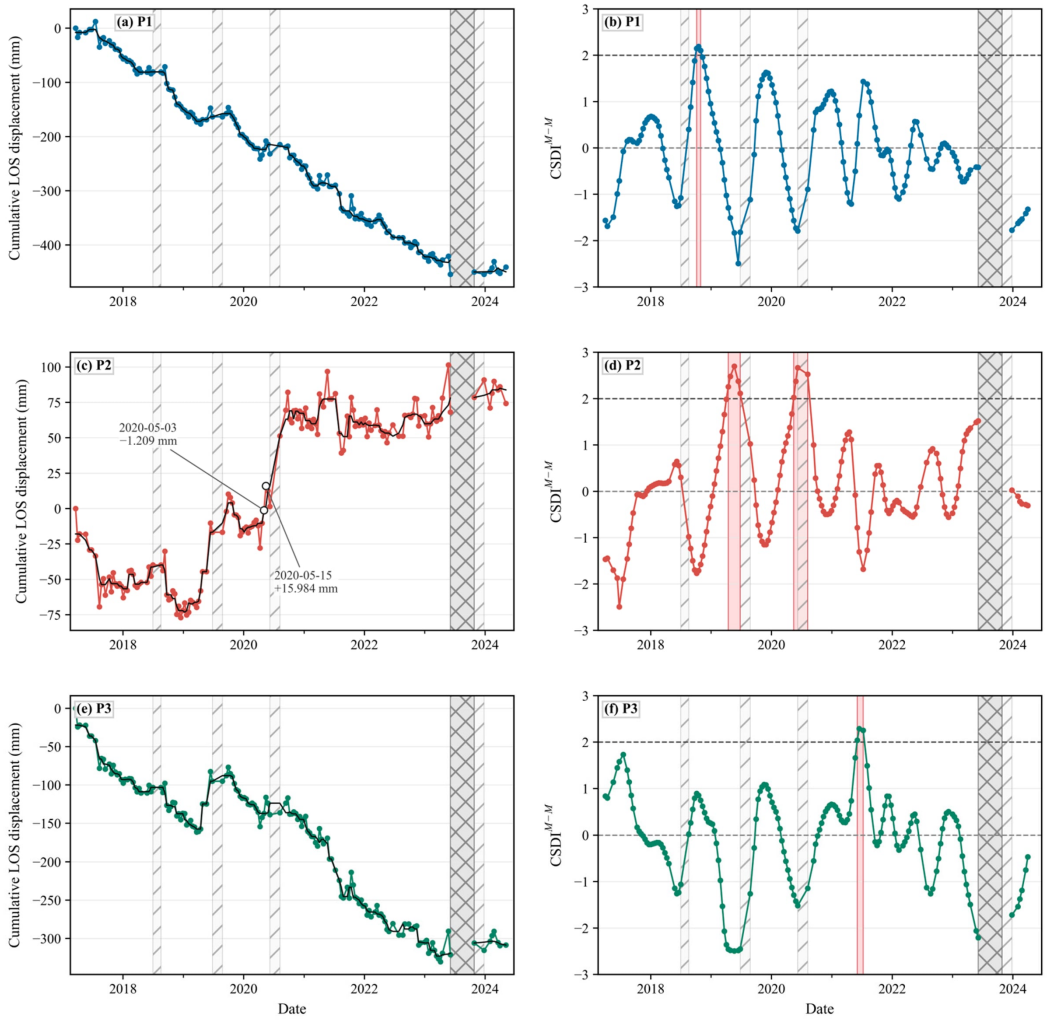


Figure 9. Ascending-track cumulative LOS displacement (**a**,**c**,**e**) and CSDI (**b**,**d**,**f**) at P1, P2, and P3, respectively. Dashed lines mark the CSDI thresholds (0 and 2); light-red shading denotes Stage III, while diagonal and cross-hatched shading indicate low-confidence (37–60 d) and hard (>60 d) observation gaps, respectively. All CSDI panels use the same vertical limits (−3 to 3). The cumulative LOS panels retain point-specific displacement ranges to show local time-series variations.

Overall, during the InSAR observation period the Li-Kan Highway landslide can be characterized as undergoing spatially differentiated kinematic adjustment superimposed on persistent deformation. Although P1 and P2 successively show episodic increases in deformation activity, and P2 locally reaches the CSDI-defined Stage III category (a statistical high-activity state) in spring–summer 2020, this high-activity state does not occur synchronously across the landslide. The long-term evolution is therefore better described as a spatially heterogeneous and temporally asynchronous process rather than as a uniform sequence of deformation stages experienced simultaneously by the entire slope.

5.2. Seasonal Deformation Fluctuations of the Li-Kan Highway Landslide

Figure 10 shows the continuous wavelet-transform results for the seasonal components of the ascending-track LOS displacement series at P1–P3 and the 12 d cumulative rainfall series prepared as described in Section 3.3. The deformation spectra characterize the time-varying power of the retained seasonal components and depend on the prescribed

decomposition period. The thin black line denotes the cone of influence, and the thick black contour encloses regions that pass the 95% confidence test against red noise. The color scale represents wavelet power, with red indicating high power and blue indicating low power. P1 exhibits a high-power band with a period of approximately one year from August 2018 to September 2022. P2 and P3 show high-power regions with periods of approximately two years from June 2019 to December 2021. Rainfall shows an approximately annual high-power band over the full time domain.

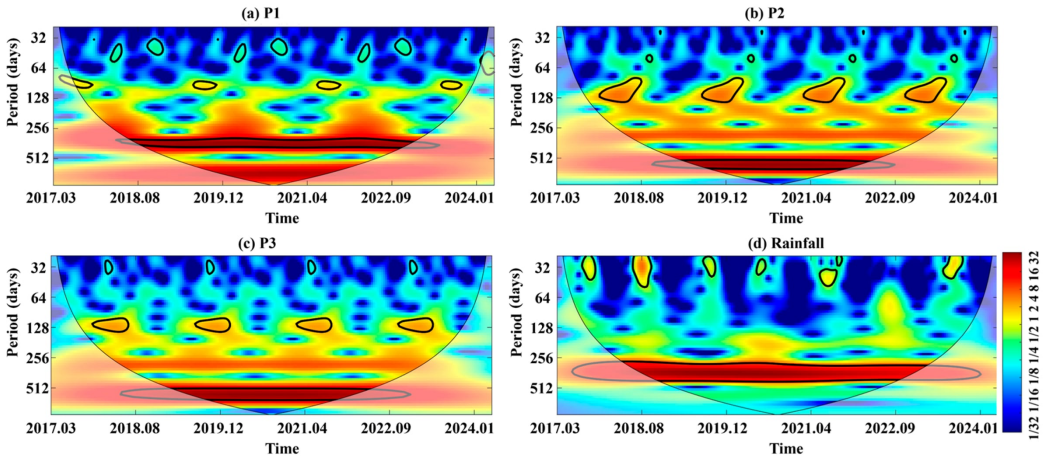


Figure 10. Individual continuous wavelet power spectra of the seasonal ascending-track LOS deformation components at (**a**) P1, (**b**) P2 and (**c**) P3, and (**d**) the matched 12 d cumulative rainfall series. The panels display single-series power rather than cross-wavelet power or wavelet coherence. All period axes are expressed in days. No inter-series phase direction is inferred from these power panels.

Figure 10 presents the individual CWT power spectra of deformation and rainfall. Similar high-power bands in separate spectra do not by themselves establish cross-series phase coherence or a lead–lag relationship [55]. No XWT or WTC phase estimate is reported here, and no inter-series phase direction is inferred from the CWT power panels. The time-domain rainfall–deformation offsets are assessed separately using TLCC.

TLCC was applied to the STL-derived seasonal deformation series x and rainfall series y, sampled at 12 d intervals. Positive lag means that rainfall leads deformation (deformation lags rainfall); negative lag means that deformation leads rainfall. At zero lag, the two series are aligned in time. The lag corresponding to the maximum absolute correlation coefficient was selected, allowing either a positive or negative correlation to identify the strongest association. These temporal associations do not establish causality.

As shown in Figure 11, the maximum-absolute-correlation peaks at P1, P2 and P3 occur at positive lags of one, nine and three sampling steps, equivalent to 12, 108 and 36 d, respectively. The corresponding correlation coefficients are +0.46, −0.54 and +0.31, respectively. The selected coefficient at P2 is negative; its absolute magnitude, rather than the largest positive correlation, determines the selected lag. At these lags, the coefficients lie outside the approximate pointwise 95% significance bounds under the stated white-noise approximation. P1 is located near the rear of the landslide, where tensile stresses typically promote crack development and higher permeability, facilitating rapid rainfall infiltration and therefore a shorter response lag. The longer lags at P2 and P3 may reflect the longer time required for infiltrating water to reach deeper zones and induce deformation. These differences in lag time may therefore be related to groundwater flow paths, sliding-zone depth, and spatial variations in permeability.

The CWT panels show single-series power and are not used to infer inter-series phase; phase-based cross-wavelet analysis (XWT/WTC) is left for future work.

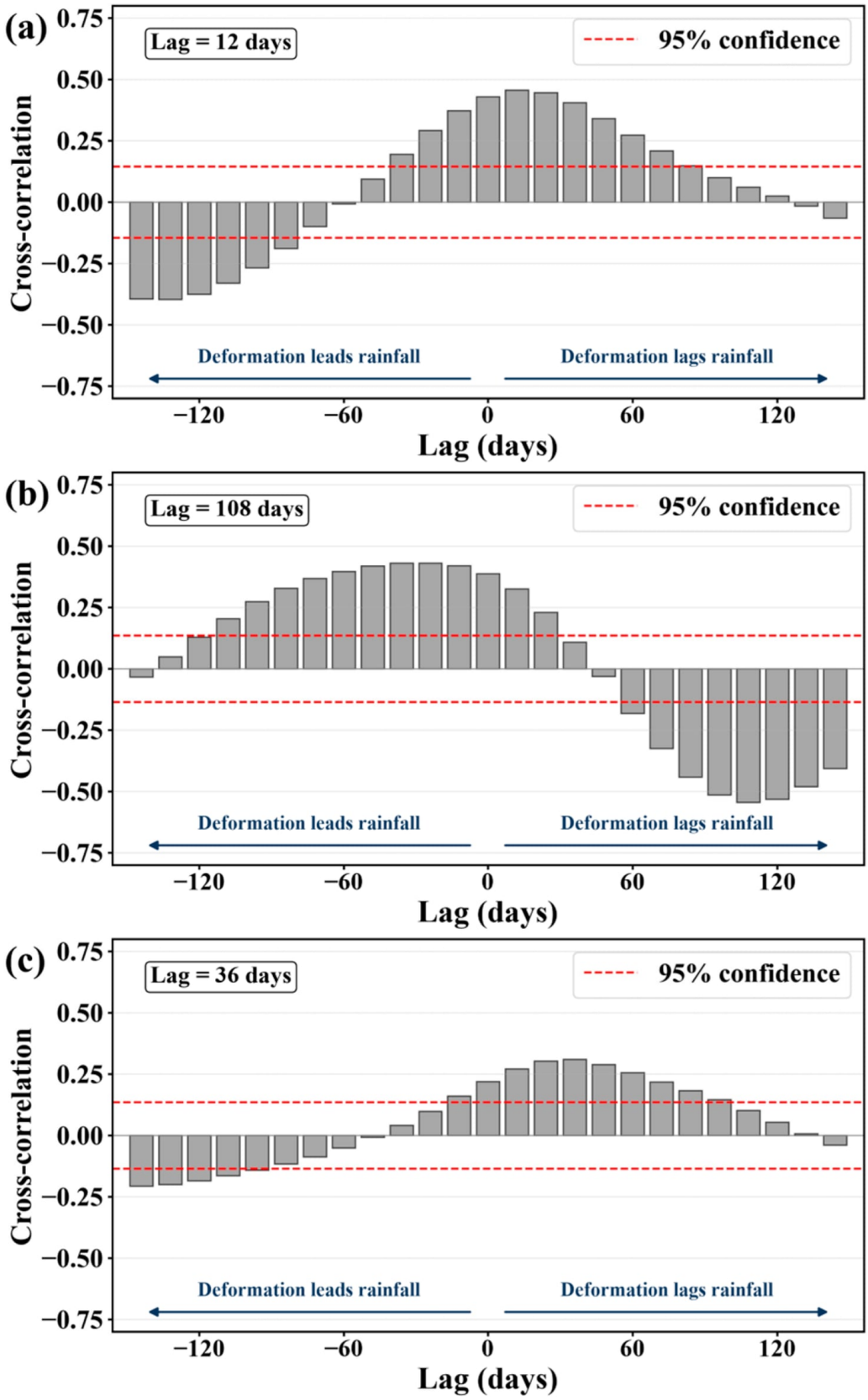


Figure 11. Time-lag cross-correlation at (**a**) P1, (**b**) P2, and (**c**) P3. Positive and negative lags indicate deformation lagging and leading rainfall, respectively. Red dashed lines denote approximate pointwise 95% significance bounds ($\pm 1.96/\sqrt{N}$) under a white-noise approximation, where N is the paired sample size for each point, held constant across lags. Coefficients outside these bounds are significant at the 95% level under this approximation.

5.3. Potential Failure Process of the Li-Kan Highway Landslide

To characterize the dynamic evolution of a potential failure mass from release in the source area, through downslope runout, to deposition at the front, the Massflow results with a 7 m grid were analyzed at six representative times (0, 10, 20, 40, 100, and 200 s). Spatial changes in landslide thickness and velocity were examined, and three representative points, M1, M2, and M3, were located in the source area, the main transport channel, and the frontal deposition zone, respectively (Figures 12 and 13). Landslide velocity was calculated from the magnitude of the horizontal velocity components. The simulation focuses on the potential failure zone at the landslide front to assess its possible runout path and deposition pattern. The initial moving mass had an area of approximately 11.84×10^4 m^2, a volume of approximately 1.26×10^6 m^3, an average thickness of 10.60 m, and a maximum thickness of 21.44 m. At 200 s, the total moving-mass volume within the computational domain had decreased by only approximately 0.38% relative to the initial value, indicating that mass was essentially conserved and that the numerical solution showed good mass conservation.

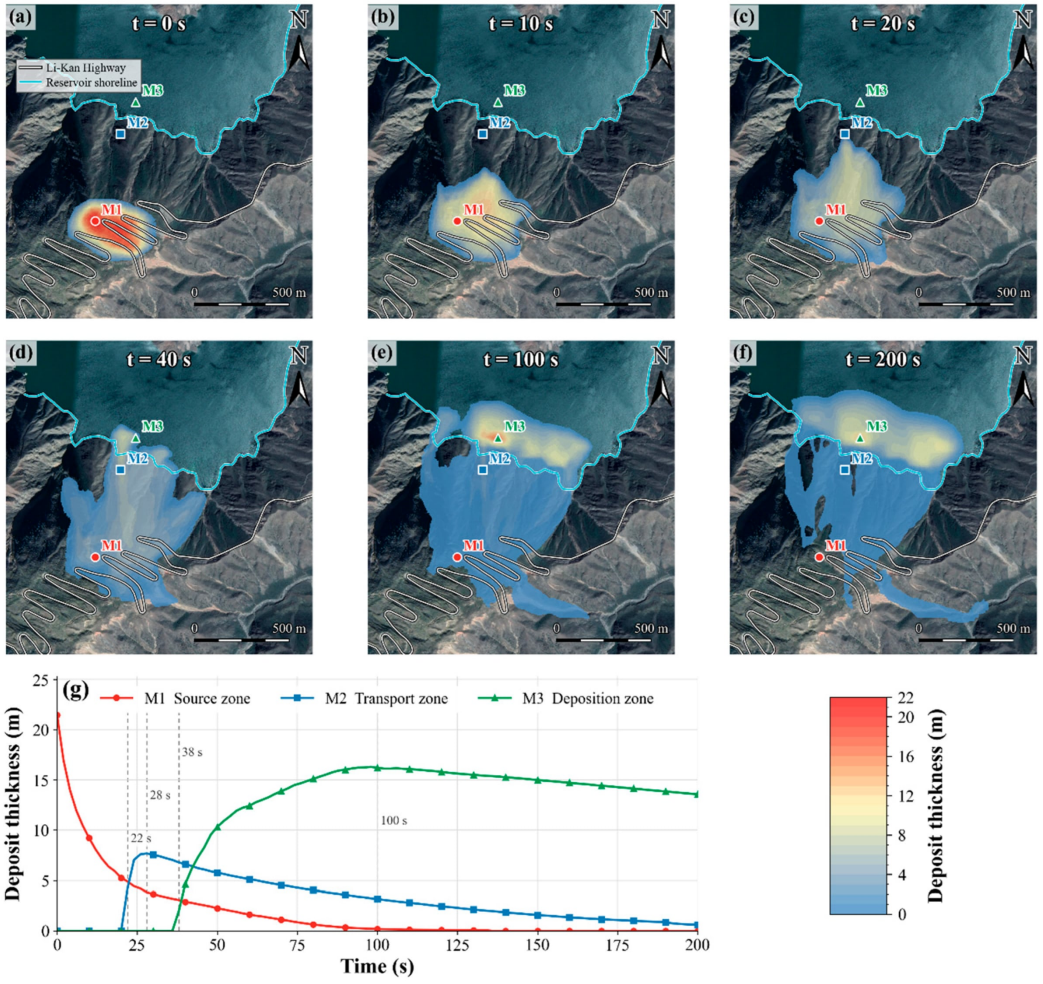


Figure 12. Spatiotemporal evolution of simulated landslide thickness at (**a**–**f**) 0, 10, 20, 40, 100 and 200 s, and (**g**) thickness time series at M1, M2 and M3. These simulation locations represent the source area, transport channel and frontal deposition zone, respectively, and are distinct from InSAR monitoring points P1–P3. The highway centerline and imagery-derived reservoir shoreline are shown. Vertical dashed lines in (**g**) mark 22, 28, 38 and 100 s. M3 lies within the reservoir footprint; results there represent numerical continuation over the fixed DEM surface without landslide–water coupling.

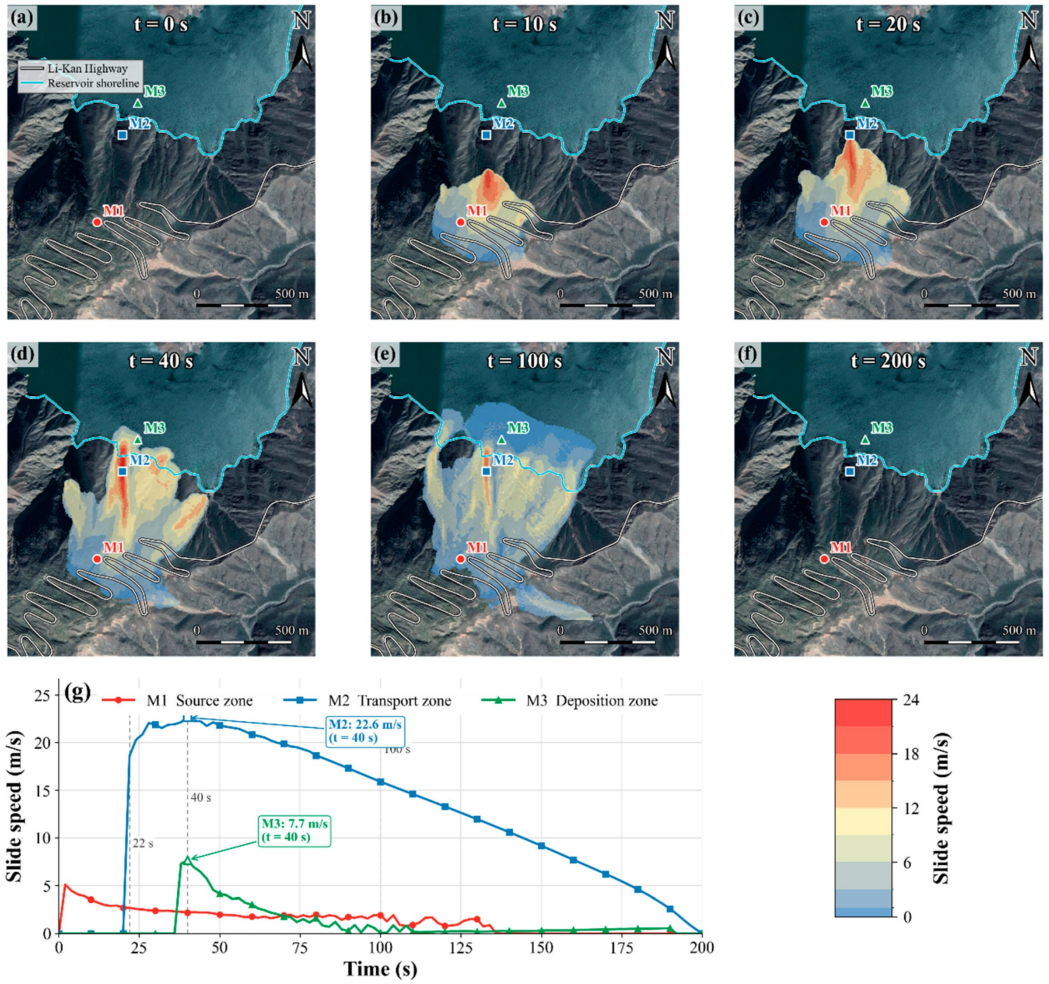


Figure 13. Spatiotemporal evolution of simulated landslide velocity at (**a**–**f**) 0, 10, 20, 40, 100 and 200 s, and (**g**) velocity time series at M1, M2 and M3. These simulation locations represent the source area, transport channel and frontal deposition zone, respectively, and are distinct from InSAR monitoring points P1–P3. The highway centerline and imagery-derived reservoir shoreline are shown. Vertical dashed lines in (**g**) mark 22, 40 and 100 s; callouts identify the approximate 40 s peaks of 22.6 m/s at M2 and 7.7 m/s at M3. M3 lies within the reservoir footprint; results there represent numerical continuation over the fixed DEM surface without landslide–water coupling.

The highway centerline and reservoir shoreline are overlaid on the runout maps in Figures 12 and 13. The shoreline represents the water–land boundary visible in the background imagery at its acquisition time. M3 lies within the reservoir footprint shown in this imagery. It is a numerical simulation sampling point, and its thickness and velocity time series are extracted from Massflow outputs rather than SAR observations; it is distinct from the InSAR monitoring point P3.

As shown in Figure 12, during 0–40 s the motion was dominated by rapid unloading of the source area and downslope spreading. At M1, the thickness rapidly decreased from the initial 21.44 m while the landslide front continued to advance downslope. As indicated by the vertical dashed reference lines in Figure 12g, M2 began to respond at approximately 22 s and reached its maximum thickness at approximately 28 s, indicating rapid passage of material through the main transport channel. As the source area continued to empty, the moving mass progressively split along topographic gullies and converged toward the slope toe and frontal zone.

From 40 to 100 s, rapid frontal deposition developed. The remaining vertical dashed reference lines in Figure 12g show that M3 began to respond at approximately 38 s, and its

thickness increased rapidly to more than 16 m at approximately 100 s, indicating substantial modeled accumulation of upslope material on the prescribed fixed surface in the frontal zone. Meanwhile, M1 continued to thin and the thickness at M2 gradually decreased, showing a clear spatial transition from source-area thinning, through channelized transport, to frontal thickening.

After 100–200 s, most material in the source area had been released, and the motion was dominated by internal adjustment and local redistribution within the deposit. After reaching its peak, the thickness at M3 slowly decreased but remained approximately 13.6 m at 200 s, forming a persistent modeled accumulation center on the prescribed fixed surface; M2 continued to thin to a low level. By 200 s, the overall spatial extent and principal depositional morphology had become essentially stable, indicating that large-scale mass transfer was nearly complete. Overall, the sequential responses at M1, M2, and M3 record the full process from source-area release, through transport along the main channel, to final frontal deposition.

Figure 13 shows that the moving mass rapidly entered a high-velocity state after initiation. M1 briefly accelerated during the initial stage and then decelerated rapidly, mainly reflecting unloading of the source area. The critical times and peak velocities described below are marked by vertical dashed reference lines and numerical callouts in Figure 13g. M2 showed a clear response at approximately 22 s and reached a maximum velocity of approximately 22.6 m/s at around 40 s, the highest value during the entire simulation, indicating pronounced velocity concentration in the main transport channel. M3 accelerated rapidly after the moving mass reached the frontal zone, attaining approximately 7.7 m/s at around 40 s before rapidly decelerating.

After 40 s, the velocity field entered an overall deceleration stage. The velocity at M2 generally decreased continuously from its peak as the moving mass spread downslope and frictional energy dissipation increased. After deposition developed at the front, the velocity at M3 rapidly decreased to a low level and, after approximately 100 s, mainly reflected low-velocity local adjustment. The approximate 100 s reference time is marked by a vertical dashed line in Figure 13g. Spatially, high-velocity zones were initially concentrated in the central gully and main transport channel and then progressively contracted. By 200 s, the effective velocity of the moving mass had nearly decreased to zero, indicating that the potential failure process had essentially ended and the mass had reached a stable depositional state.

In the present simulation, reservoir water is not represented as a separate fluid layer. The moving mass is calculated over the fixed surface prescribed by the input DEM. For valid computational cells overlapping the reservoir footprint, the model continues to solve the same depth-averaged mass and momentum conservation equations with the same Coulomb resistance parameters used elsewhere in the domain. Crossing the shoreline shown in the background imagery does not activate a separate landslide–water interaction calculation. Explicit buoyancy, hydrodynamic drag, and momentum exchange between the moving mass and reservoir water are therefore not included.

Based on the combined thickness and velocity evolution, the potential failure process can be divided into four stages: initiation and release, high-speed runout, flow splitting and spreading, and deceleration and deposition. The simulation indicates that, once initiated, the potential failure mass at the front of the Li-Kan Highway landslide could rapidly move downslope along preferential gullies toward the slope toe and reservoir shoreline. The maximum velocity in the central transport channel exceeds 20 m/s. Because the current model does not account for erosion and entrainment or hydrodynamic coupling after the moving mass enters the reservoir, the simulation results are mainly used to identify potential runout paths and high-intensity zones. Results within the reservoir footprint, including M3,

represent numerical continuation over the prescribed fixed surface and are not predictions of actual underwater motion, reservoir-bed deposition, or landslide-generated waves.

Reservoir-level fluctuations may change hydrostatic loading at the slope toe and the hydraulic gradient within the slope. During drawdown, external water support can decrease before internal pore pressures dissipate. Changes in reservoir level can therefore interact with rainfall infiltration and produce delayed deformation responses, depending on slope permeability and drainage [61]. These mechanisms are potential influences at Li-Kan, rather than effects established from site-specific water-level observations.

No continuous reservoir-level record covering the InSAR observation period was available. Consequently, the amplitude, rate and timing of reservoir-level changes could not be compared with the measured deformation, and the respective contributions of rainfall and reservoir operation could not be separated. The 2180 m normal water level in Figure 1 and the shoreline visible in the September 2022 imagery are reference information, not a reconstruction of reservoir levels throughout the monitoring period. The rainfall–deformation associations therefore do not establish rainfall as the sole trigger. Matched reservoir-level, groundwater and deformation observations are needed to test these potential mechanisms.

6. Conclusions

In this paper, ascending and descending track time-series InSAR, APF-constrained three-dimensional deformation reconstruction, CSDI, wavelet and time-lag analyses, and Massflow numerical simulation were integrated to investigate the spatiotemporal evolution, rainfall response, and potential failure process of the Li-Kan Highway landslide. The main conclusions can be summarized as follows:

(1) The APF-constrained integration of ascending- and descending-track InSAR effectively reconstructs the three-dimensional deformation pattern of the Li-Kan Highway landslide. The horizontal motion is predominantly northeastward, whereas local sectors exhibit different movement directions and deformation components, indicating the presence of multiple kinematic units. Along the approximately 2 km P–P′ transect, the NS, EW, and UD velocity components show heterogeneous spatial variations. Local variations in the APF-derived velocity profiles alone do not establish independently verified sliding-unit boundaries. In addition, PC1 and PC2 together explain 85.6% of the total variance, providing a compact description of deformation variability.

(2) CSDI analysis reveals pronounced temporal asynchrony among different parts of the landslide. Enhanced deformation activity occurs mainly at P1 in autumn 2018, at P2 in 2019 and spring–summer 2020, and more weakly at P3 around mid-2021. The marked response at P2 in 2020 is better interpreted as a local kinematic adjustment rather than synchronous acceleration of the entire landslide. Therefore, the long-term evolution of the Li-Kan Highway landslide is characterized by persistent deformation combined with spatially differentiated and temporally asynchronous activity. Because no overall failure occurred during the observation period, locally identified CSDI Stage III intervals should be interpreted as enhanced deformation activity rather than direct evidence of imminent failure.

(3) Wavelet and time-lag cross-correlation analyses indicate spatially variable rainfall responses within the landslide. P1 shows an approximately annual deformation cycle, whereas P2 and P3 exhibit relatively strong longer-period components during part of the observation period. Deformation at P1, P2, and P3 lags rainfall by approximately 12, 108, and 36 days, respectively. These differences suggest that rainfall-induced deformation does not occur uniformly across the slope and may be controlled by spatial variations in crack development, infiltration pathways, sliding-zone depth,

and permeability. These associations do not isolate rainfall effects from potential reservoir-level effects, for which continuous site records were unavailable.

(4) Massflow simulation shows that the potential failure process at the landslide front can be divided into four stages: initiation and release, high-speed runout, flow splitting and spreading, and deceleration and deposition. The maximum simulated velocity reaches approximately 22.6 m/s in the main transport channel, while the simulated thickness at the frontal sampling point M3 exceeds 16 m and remains approximately 13.6 m at 200 s. The total simulated mass decreases by only approximately 0.38%, indicating good numerical mass conservation. The results indicate potential runout paths toward the slope toe and reservoir shoreline and associated high-intensity zones. Because erosion, entrainment and hydrodynamic coupling were not considered, results within the reservoir footprint, including M3, represent numerical continuation over the prescribed fixed surface and do not predict actual underwater motion, reservoir-bed deposition or landslide-generated waves.

Future work will extend the present time-domain lag analysis with cross-wavelet transform and wavelet coherence using longer, gap-filled records, and will combine it with continuous reservoir-level and groundwater observations to separate rainfall from reservoir effects. Incorporating erosion–entrainment and landslide–water coupling into the runout model would further improve predictions of post-failure motion within the reservoir.

Author Contributions: Conceptualization, Y.W. and Y.Z.; methodology, Y.W. and X.L.; software, X.L.; validation, Y.W.; formal analysis, H.G.; investigation, Z.P. and X.L.; resources, Y.Z.; data curation, W.Z.; writing—original draft preparation, Y.W.; writing—review and editing, Y.W., Y.Z., Z.P., H.G., X.L. and W.Z.; visualization, H.G.; supervision, W.Z.; project administration, Z.P.; funding acquisition, W.Z. All authors have read and agreed to the published version of the manuscript.

Funding: This work was supported in part by the Yunnan Provincial Key Research and Development Program Project under Grant 202603AG380001 and 202403AA080011; in part by the Natural Science Foundation of China under Grant 42474051 and 42074040; in part by the Shaanxi Provincial Key Research and Development Program under Grant 2026CY-ZDGG-89; in part by the Natural Science Basic Research Plan in Shaanxi Province of China under Grant 2023-JC-JQ-24; in part by the Fundamental Research Funds for the Central Universities, CHD under Grant 300102265302; and in part by the Local Service Special Project of Shaanxi Provincial Department of Education under Grant 25JE004.

Data Availability Statement: The raw data supporting the conclusions of this article will be made available by the authors on request.

Acknowledgments: We would like to thank the reviewers for their helpful comments.

Conflicts of Interest: The authors declare no conflicts of interest.

References

1. Derbyshire, E. Geological Hazards in Loess Terrain, with Particular Reference to the Loess Regions of China. *Earth Sci. Rev.* **2001**, *54*, 231–260. [CrossRef]
2. Juang, C.H.; Dijkstra, T.; Wasowski, J. Loess Geohazards Research in China: Advances and Challenges for Mega Engineering Projects. *Eng. Geol.* **2019**, *251*, 1–10. [CrossRef]
3. Xu, Y.; Allen, M.B.; Zhang, W. Landslide Characteristics in the Loess Plateau, Northern China. *Geomorphology* **2020**, *359*, 107150. [CrossRef]
4. Casagli, N.; Frodella, W.; Morelli, S.; Tofani, V.; Ciampalini, A.; Intrieri, E.; Raspini, F.; Rossi, G.; Tanteri, L.; Lu, P. Spaceborne, UAV and Ground-Based Remote Sensing Techniques for Landslide Mapping, Monitoring and Early Warning. *Geoenviron. Disasters* **2017**, *4*, 9. [CrossRef]
5. Novellino, A.; Pennington, C.; Leeming, K.; Taylor, S.; Gonzalez Alvarez, I.; McAllister, E.; Arnhardt, C.; Winson, A. Mapping Landslides from Space: A Review. *Landslides* **2024**, *21*, 1041–1052. [CrossRef]
6. Gabriel, A.K.; Goldstein, R.M.; Zebker, H.A. Mapping Small Elevation Changes over Large Areas: Differential Radar Interferometry. *J. Geophys. Res. Solid Earth* **1989**, *94*, 9183–9191. [CrossRef]

7. Ferretti, A.; Prati, C.; Rocca, F. Nonlinear Subsidence Rate Estimation Using Permanent Scatterers in Differential SAR Interferometry. *IEEE Trans. Geosci. Remote Sens.* **2000**, *38*, 2202–2212. [CrossRef]
8. Berardino, P.; Fornaro, G.; Lanari, R.; Sansosti, E. A New Algorithm for Surface Deformation Monitoring Based on Small Baseline Differential SAR Interferograms. *IEEE Trans. Geosci. Remote Sens.* **2002**, *40*, 2375–2383. [CrossRef]
9. Crosetto, M.; Monserrat, O.; Cuevas-González, M.; Devanthéry, N.; Crippa, B. Persistent Scatterer Interferometry: A Review. *ISPRS J. Photogramm. Remote Sens.* **2016**, *115*, 78–89. [CrossRef]
10. Wasowski, J.; Bovenga, F. Investigating Landslides and Unstable Slopes with Satellite Multi Temporal Interferometry: Current Issues and Future Perspectives. *Eng. Geol.* **2014**, *174*, 103–138. [CrossRef]
11. Fruneau, B.; Achache, J.; Delacourt, C. Observation and Modelling of the Saint-Étienne-de-Tinée Landslide Using SAR Interferometry. *Tectonophysics* **1996**, *265*, 181–190. [CrossRef]
12. Yi, Y.; Xu, X.; Xu, G.; Gao, H. Landslide Detection Using Time-Series InSAR Method along the Kangding-Batang Section of Shanghai-Nyalam Road. *Remote Sens.* **2023**, *15*, 1452. [CrossRef]
13. Liu, Z.; Qiu, H.; Zhu, Y.; Liu, Y.; Yang, D.; Ma, S.; Zhang, J.; Wang, Y.; Wang, L.; Tang, B. Efficient Identification and Monitoring of Landslides by Time-Series InSAR Combining Single- and Multi-Look Phases. *Remote Sens.* **2022**, *14*, 1026. [CrossRef]
14. Zhou, Y.; Liu, X.; Zhu, W.; Wang, Y.; Wei, Z.; Wu, J.; Shang, H.; Yang, T.; Du, C. Spatial Clustering and Controlling Factors of Active Landslides in the Upper Yellow River: Insights from SBAS-InSAR and XGBoost–SHAP Modeling. *IEEE J. Sel. Top. Appl. Earth Obs. Remote Sens.* **2026**, *19*, 19307–19322. [CrossRef]
15. Liu, X.; Zhao, C.; Zhang, Q.; Yin, Y.; Lu, Z.; Samsonov, S.; Yang, C.; Wang, M.; Tomás, R. Three-Dimensional and Long-Term Landslide Displacement Estimation by Fusing C- and L-Band SAR Observations: A Case Study in Gongjue County, Tibet, China. *Remote Sens. Environ.* **2021**, *267*, 112745. [CrossRef]
16. Du, J.T.; Song, C.; Li, Z.H.; Tomás, R.; Li, Z. Kinematic Behavior and Sliding Geometry of Large Anthropogenic-Induced Landslides Using Three-Dimensional Time Series InSAR: Insights from the Li-Kan Road Landslide. *Landslides* **2025**, *22*, 3319–3333. [CrossRef]
17. Saito, M. Forecasting the Time of Occurrence of a Slope Failure. In Proceedings of the 6th International Conference on Soil Mechanics and Foundation Engineering, Montreal, QC, Canada, 8–15 September 1965; pp. 537–541.
18. Xu, Q.; Tang, M.G.; Xu, K.X.; Huang, X.B. Research on Space-Time Evolution Laws and Early Warning-Prediction of Landslides. *Chin. J. Rock Mech. Eng.* **2008**, *27*, 1104–1112. (In Chinese) [CrossRef]
19. Xu, Q.; Zeng, Y.P.; Qian, J.P.; Wang, C.J.; He, C.J. Study on an Improved Tangential Angle and the Corresponding Landslide Pre-Warning Criteria. *Geol. Bull. China* **2009**, *28*, 501–505. (In Chinese) [CrossRef]
20. Liu, X.S.; Luo, W.Q.; Li, F.A.; Huang, L. Identification Index of Landslide Evolution Stage Based on Association Rule. *Geol. Sci. Technol. Inf.* **2014**, *33*, 160–164. (In Chinese) [CrossRef]
21. Huang, L.; Fan, X.J.; Luo, W.Q. Division of Landslide Evolution Stages Based on the Optimal Segmentation Algorithm of Ordered Samples. *J. Hubei Univ. Arts Sci.* **2015**, *36*, 13–16. (In Chinese)
22. Bao, L.; Zhang, G.; Hu, X.; Wu, S.; Liu, X. Stage Division of Landslide Deformation and Prediction of Critical Sliding Based on Inverse Logistic Function. *Energies* **2021**, *14*, 1091. [CrossRef]
23. Chen, Y.; Ye, R.; Yi, Q.; Zu, Q.; Wu, Z. Step-like Landslides Warning Method Based on Feature Point Analysis of Monitoring Curve. *South China Geol.* **2023**, *39*, 523–535. (In Chinese)
24. Wang, L.W.; Xie, M.W.; Chai, X.Q. Research on Method of Displacement Speed Ratio for Spatial Evaluation of Landslide Deformation. *Rock Soil Mech.* **2014**, *35*, 519–528. (In Chinese)
25. Zhang, J.; Tang, H.; Li, C.; Gong, W.; Zhou, B.; Zhang, Y. Deformation stage division and early warning of landslides based on the statistical characteristics of landslide kinematic features: Zhang et al. *Landslides* **2024**, *21*, 717–735. [CrossRef]
26. Zhu, W.; He, Q.; Wu, J.; Wang, Y.; Li, Z.; Zhan, J.; Zhang, B. Identifying Reservoir Landslide Deformation Evolution Stages with Time Series InSAR: Application to the Xinpu Landslide in China's Three Gorges Region. *J. Hydrol.* **2025**, *663*, 134136. [CrossRef]
27. Yang, B.; Liu, Z.; Lacasse, S.; Wang, L.; Xiao, T. Deformation Triggers and Stability Evolution of Landslide from Multiple Observations. *Front. Ecol. Evol.* **2023**, *11*, 1242093. [CrossRef]
28. Liu, Y.; Qiu, H.; Yang, D.; Liu, Z.; Ma, S.; Pei, Y.; Zhang, J.; Tang, B. Deformation Responses of Landslides to Seasonal Rainfall Based on InSAR and Wavelet Analysis. *Landslides* **2022**, *19*, 199–210. [CrossRef]
29. Xia, Z.; Motagh, M.; Wang, W.; Li, T.; Peng, M.; Zhou, C.; Karimzadeh, S. Modeling Slope Instabilities with Multi-Temporal InSAR Considering Hydrogeological Triggering Factors: A Case Study across Badong County in the Three Gorges Area. *Remote Sens. Environ.* **2024**, *309*, 114212. [CrossRef]
30. Ren, S.; Zhang, Y.; Li, J.; Zhou, Z.; Liu, X.; Tao, C. Deformation Behavior and Reactivation Mechanism of the Dandu Ancient Landslide Triggered by Seasonal Rainfall: A Case Study from the East Tibetan Plateau, China. *Remote Sens.* **2023**, *15*, 5538. [CrossRef]
31. Savage, S.B.; Hutter, K. The Motion of a Finite Mass of Granular Material down a Rough Incline. *J. Fluid Mech.* **1989**, *199*, 177–215. [CrossRef]
32. Hungr, O. A Model for the Runout Analysis of Rapid Flow Slides, Debris Flows, and Avalanches. *Can. Geotech. J.* **1995**, *32*, 610–623. [CrossRef]

33. Iverson, R.M. The Physics of Debris Flows. *Rev. Geophys.* **1997**, *35*, 245–296. [CrossRef]
34. Iverson, R.M.; Denlinger, R.P. Flow of Variably Fluidized Granular Masses across Three-Dimensional Terrain: 1. Coulomb Mixture Theory. *J. Geophys. Res. Solid Earth* **2001**, *106*, 537–552. [CrossRef]
35. Pudasaini, S.P. A General Two-Phase Debris Flow Model. *J. Geophys. Res. Earth Surf.* **2012**, *117*, F03010. [CrossRef]
36. Mergili, M.; Fischer, J.-T.; Krenn, J.; Pudasaini, S.P. r.avaflow v1, an Advanced Open-Source Computational Framework for the Propagation and Interaction of Two-Phase Mass Flows. *Geosci. Model Dev.* **2017**, *10*, 553–569. [CrossRef]
37. McDougall, S.; Hungr, O. A Model for the Analysis of Rapid Landslide Motion across Three-Dimensional Terrain. *Can. Geotech. J.* **2004**, *41*, 1084–1097. [CrossRef]
38. Hungr, O.; McDougall, S. Two Numerical Models for Landslide Dynamic Analysis. *Comput. Geosci.* **2009**, *35*, 978–992. [CrossRef]
39. Ouyang, C.; He, S.; Xu, Q.; Luo, Y.; Zhang, W. A MacCormack-TVD Finite Difference Method to Simulate the Mass Flow in Mountainous Terrain with Variable Computational Domain. *Comput. Geosci.* **2013**, *52*, 1–10. [CrossRef]
40. Ouyang, C.; He, S.; Tang, C. Numerical Analysis of Dynamics of Debris Flow over Erodible Beds in Wenchuan Earthquake-Induced Area. *Eng. Geol.* **2015**, *194*, 62–72. [CrossRef]
41. Ouyang, C.; Zhou, K.; Xu, Q.; Yin, J.; Peng, D.; Wang, D.; Li, W. Dynamic Analysis and Numerical Modeling of the 2015 Catastrophic Landslide of the Construction Waste Landfill at Guangming, Shenzhen, China. *Landslides* **2017**, *14*, 705–718. [CrossRef]
42. Zhu, W.; Yang, L.; Cheng, Y.; Liu, X.; Zhang, R. Active Thickness Estimation and Failure Simulation of Translational Landslide Using Multi-Orbit InSAR Observations: A Case Study of the Xiongba Landslide. *Int. J. Appl. Earth Obs. Geoinf.* **2024**, *129*, 103801. [CrossRef]
43. Ma, S.; Qiu, H.; Zhu, Y.; Yang, D.; Tang, B.; Wang, D.; Wang, L.; Cao, M. Topographic Changes, Surface Deformation and Movement Process before, during and after a Rotational Landslide. *Remote Sens.* **2023**, *15*, 662. [CrossRef]
44. Gu, Z.; Xin, P.; Yao, X.; Cao, S. Multi-Field Coupling Early Warning of Climate-Induced Cascading Landslide Hazards: The Likan Landslides in the Upper Yellow River, China. *Int. J. Appl. Earth Obs. Geoinf.* **2026**, *147*, 105198. [CrossRef]
45. Feng, W.G.; Du, J.H. Causes and Treatment of Likan Highway No. 1 Landslide. *Qinghai Transp. Sci. Technol.* **2003**, 25–29. (In Chinese)
46. Luo, Y.T.; Xu, F.; Bai, Z.L. Characteristics, Causes and Deformation Mechanism of the Loess Landslide on the Right Bank of Lijiaxia Hydropower Station. *Yellow River* **2022**, *44*, 143–146. (In Chinese) [CrossRef]
47. Ying, Z.M.; Chen, J.Q.; Xu, Q. Effects of Lijiaxia Reservoir on Meteorological Element Changes in Jianzha Area. *J. Agric. Catastrophol.* **2021**, *11*, 35–36. (In Chinese)
48. Samsonov, S.V. Multidimensional Small Baseline Subset (MSBAS) Software for Constrained and Unconstrained Deformation Analysis of Partially Coherent DInSAR and Speckle Offset Data. *Can. J. Remote Sens.* **2024**, *50*, 2424753. Correction in *Can. J. Remote Sens.* **2025**, *51*, 2493404. [CrossRef]
49. Morishita, Y.; Kobayashi, T. Three-Dimensional Deformation and Its Uncertainty Derived by Integrating Multiple SAR Data Analysis Methods. *Earth Planets Space* **2022**, *74*, 16. [CrossRef]
50. Sharifi, S.; Macciotta, R.; Hendry, M.; Rotheram-Clarke, D.; Huntley, D. Evaluating Topography-Based Methods in 3D Decomposition of InSAR 1D Velocities Obtained for Translational Landslides: Thompson River Valley in Canada. *Landslides* **2024**, *21*, 411–427. [CrossRef]
51. Hu, X.; Lu, Z.; Pierson, T.C.; Kramer, R.; George, D.L. Combining InSAR and GPS to Determine Transient Movement and Thickness of a Seasonally Active Low-Gradient Translational Landslide. *Geophys. Res. Lett.* **2018**, *45*, 1453–1462. [CrossRef]
52. Cleveland, R.B.; Cleveland, W.S.; McRae, J.E.; Terpenning, I. STL: A Seasonal-Trend Decomposition Procedure Based on Loess. *J. Off. Stat.* **1990**, *6*, 3–73.
53. Huang, S.; Mei, G.; Sun, Y. Environmental Controls and Transition of the Baige Landslide Deformation Revealed by Time-Series Remote Sensing Observations. *Remote Sens.* **2026**, *18*, 2169. [CrossRef]
54. Tomás, R.; Pastor, J.L.; Béjar-Pizarro, M.; Bonì, R.; Ezquerro, P.; Fernández-Merodo, J.A.; Guardiola-Albert, C.; Herrera, G.; Meisina, C.; Teatini, P.; et al. Wavelet Analysis of Land Subsidence Time-Series: Madrid Tertiary Aquifer Case Study. *Proc. Int. Assoc. Hydrol. Sci.* **2020**, *382*, 353–359. [CrossRef]
55. Torrence, C.; Compo, G.P. A Practical Guide to Wavelet Analysis. *Bull. Am. Meteorol. Soc.* **1998**, *79*, 61–78. [CrossRef]
56. Yao, H.Y. Prediction of Single-Site PM2.5 Concentration Based on Machine Learning and Its Spatiotemporal Influencing Factors. Master's Thesis, East China Normal University, Shanghai, China, 2022. (In Chinese)
57. Iverson, R.M.; Ouyang, C. Entrainment of Bed Material by Earth-Surface Mass Flows: Review and Reformulation of Depth-Integrated Theory. *Rev. Geophys.* **2015**, *53*, 27–58. [CrossRef]
58. Cui, Y.; Qian, Z.; Xu, W.; Xu, C. A Small-Scale Landslide in 2023, Leshan, China: Basic Characteristics, Kinematic Process and Cause Analysis. *Remote Sens.* **2024**, *16*, 3324. [CrossRef]
59. Ouyang, C.; An, H.; Zhou, S.; Wang, Z.; Su, P.; Wang, D.; Cheng, D.; She, J. Insights from the Failure and Dynamic Characteristics of Two Sequential Landslides at Baige Village along the Jinsha River, China. *Landslides* **2019**, *16*, 1397–1414. [CrossRef]

60. Zhao, S.; Zeng, R.; Zhang, Z.; Meng, X.; Wei, Z.; Wang, X.; Long, Z.; Liu, Y.; Chen, H. Prediction of Movement Trajectories and Surge Disaster-Affected Areas Following Instability and Failure of a Large, High-Positioned, Loess–Mudstone Interface Landslide. *Bull. Eng. Geol. Environ.* **2026**, *85*, 386. [CrossRef]
61. Tang, M.G.; Li, S.L.; Xu, Q.; Gong, Z.F.; Zhu, Q.; Wei, Y. Study of Deformation Characteristics of Reservoir Landslide Based on Centrifugal Model Test. *Rock Soil Mech.* **2020**, *41*, 755–764. (In Chinese) [CrossRef]

Disclaimer/Publisher's Note: The statements, opinions and data contained in all publications are solely those of the individual author(s) and contributor(s) and not of MDPI and/or the editor(s). MDPI and/or the editor(s) disclaim responsibility for any injury to people or property resulting from any ideas, methods, instructions or products referred to in the content.